Linear and nonlinear theory of cyclotron autoresonance masers with multiple waveguide modes

Chiping Chen and Jonathan S. Wurtele
Plasma Fusion Center and Department of Physics, Massachusetts Institute of Technology, Cambridge, Massachusetts 02139

The interaction of multiple waveguide modes with a relativistic electron beam in an overmoded, single-frequency, cyclotron autoresonance maser amplifier is analyzed using a nonlinear self-consistent model and kinetic theory. It is shown analytically, and confirmed by simulation, that all of the coupled waveguide modes grow at the spatial growth rate of the dominant unstable mode, but suffer different launching losses which depend upon detuning. The phases of coupled modes are locked in the exponential gain regime, and remain approximately locked for some finite interaction length beyond saturation. The saturated power in each mode is found to be insensitive to the input modal radio-frequency (rf) power distribution, but sensitive to detuning. Simulations indicate that the saturated fractional rf power in a given mode reaches a maximum at its resonant magnetic field, and then decreases rapidly off resonance. Good agreement is found between the simulations and the kinetic theory in the linear regime.

I. INTRODUCTION

The linear and nonlinear interaction of multiple electromagnetic eigenmodes with relativistic charged particle beams has been the subject of active research in the generation of coherent radiation using free electrons. Multimode phenomena occur in oscillator as well as in amplifier configurations. In oscillator systems, such as free-electron laser (FEL) oscillators[1-3] and gyrotrons,[4] mode competition determines the temporal behavior of the eigenmodes of the cavity and the radiation spectrum. In an overmoded, single-frequency amplifier, the temporal dependence of the eigenmodes is nearly sinusoidal, but the eigenmodes evolve spatially as the interaction length increases. A nonlinear, multimode theory is indispensable in order to predict the radiation power in each mode and the transverse field profile.

Multimode interactions have been investigated using linear theory[5] and computer simulations[6] for FEL amplifiers, but detailed comparison between theory and simulations are not (yet) available. Recently, Schill[7,8] and Seshadri[8] have developed a linear kinetic theory of multimode cyclotron resonance masers. Also, competition among absolutely unstable modes has been investigated using simulation techniques.[9] There have been few theoretical studies of the nonlinear interaction of multiple *convective* waveguide modes and the electron beam in overmoded cyclotron autoresonance maser (CARM) amplifiers. The goal of this paper is to develop a formalism that can treat the linear and nonlinear evolution of an overmoded, single-frequency CARM system with an arbitrary number of transverse-electric (TE) and transverse-magnetic (TM) waveguide modes coupling to the electron beam. The preliminary results of this paper have been reported earlier.[10]

The CARM interaction[11,12] occurs when a relativistic electron beam undergoing cyclotron motion in a uniform magnetic field $B_0 e_z$ interacts with a copropagating electromagnetic wave (ω, k). The cyclotron resonance condition is $\omega = k_z v_z + l\Omega_c/\gamma$. Here, v_z and γ are, respectively, the axial velocity and relativistic mass factor of the beam electrons; l is the harmonic number; $\Omega_c = eB_0/m_0 c$ is the nonrelativistic cyclotron frequency; m_0 and $-e$ are the electron mass and charge, respectively; and c is the speed of light *in vacuo*.

The physics of CARM's[13-15] has been studied theoretically and experimentally. Experimental results on CARM oscillators[16,17] and amplifiers[18,19] have been reported recently. Theoretical work has included one-dimensional linear and nonlinear theory,[20,21] three-dimensional linear and nonlinear theory of the CARM interaction with a single TE or TM waveguide mode,[12,22] nonlinear efficiency studies,[11] the investigation of efficiency enhancement by magnetic field tapering,[21,23] the stability calculation of absolute instabilities,[24] the stabilization of the CARM maser instability by an intense electron beam,[25] and the studies of radiation guiding.[26]

In this paper, we present a general treatment of multimode interactions in an overmoded single-frequency CARM amplifier. The present analysis consists of two approaches: linear kinetic theory and computer simulations based on a fully nonlinear, three-dimensional, self-consistent model. The Maxwell–Vlasov equations are linearized to derive amplitude equations for the coupled waveguide modes in the small-signal regime. The amplitude equations are solved with the Laplace transform techniques, resulting in a dispersion relation with cyclotron harmonics and an arbitrary number of TE and TM modes. The Laplace transform analysis allows for analytical calculation of launching losses and the three-dimensional field profile (amplitude and phase). A complete set of ordinary differential equations describing the nonlinear, self-consistent evolution of the waveguide modes and of the relativistic electron beam are derived, and integrated numerically for a wide range of sys-

tem parameters. Detailed comparisons between theory and simulations are made. The general features of the linear and nonlinear multimode interaction are illustrated.

It is shown analytically, and confirmed by simulation, that all of the coupled waveguide modes grow with the dominant unstable mode at the same spatial growth rate, but suffer different launching losses which depend upon detuning characteristics. The phases of coupled modes are locked in the exponential gain regime, and remain approximately locked for some finite interaction length beyond saturation. The saturated rf power in each mode is found to be insensitive to input power distribution, but sensitive to detuning. Simulations indicate that the saturated fractional power for a given mode reaches a maximum at its resonant magnetic field, and then decreases rapidly off resonance. In the transition from one resonance to another, however, adjacent competing modes can have comparable rf power levels at saturation.

The organization of this paper is as follows. After formulating the problem in Sec. II, the Maxwell–Vlasov equations are used to derive the linearized amplitude equations and dispersion relation for the multimode CARM interaction in Sec. III. In Sec. IV, nonlinear CARM equations are derived from the standpoint of particle–wave interactions. In Sec. V, the single-mode CARM interaction is reviewed briefly in the linear and nonlinear regimes. In Sec. VI, the linear and nonlinear evolution of CARM amplifiers with two or more waveguide modes is analyzed, and the general features of multimode phenomena are illustrated.

II. GENERAL FORMULATION OF THE PROBLEM

We consider a relativistic electron beam undergoing cyclotron motion in an applied uniform magnetic field $B_0 \mathbf{e}_z$ and propagating axially through a cylindrical, perfectly conducting waveguide of radius r_w (Fig. 1). The dynamics of each individual electron is described by the Lorentz force equation

$$\frac{d\mathbf{p}}{dt} = -e\left(\mathbf{E} + \frac{\mathbf{v}}{c} \times (B_0 \mathbf{e}_z + \mathbf{B})\right), \qquad (1)$$

and the evolution of the electron beam is described by the Vlasov equation

$$\frac{\partial f}{\partial t} + \mathbf{v} \cdot \frac{\partial f}{\partial \mathbf{x}} - e\left(\mathbf{E} + \frac{\mathbf{v}}{c} \times (B_0 \mathbf{e}_z + \mathbf{B})\right) \cdot \frac{\partial f}{\partial \mathbf{p}} = 0. \qquad (2)$$
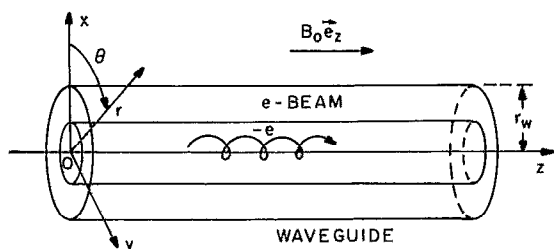
Here, $f(\mathbf{x}, \mathbf{p}, t)$ is the electron phase-space density function. In the present CARM amplifier theory, the temporal dependence of the electromagnetic perturbations $\mathbf{E}(\mathbf{x}, t)$ and $\mathbf{B}(\mathbf{x}, t)$ in Eqs. (1) and (2) are assumed to be *sinusoidal* and consist of TE and TM waveguide modes. Because the transverse field components of a TE or TM waveguide mode can be expressed in terms of the axial magnetic or electric field of that mode [see Eqs. (8)–(11)], it is sufficient to work with the axial component of the wave equation. It is readily shown from Maxwell's equations that the axial field components of the TE and TM perturbations satisfy the wave equations[12]

$$\left(\frac{d^2}{dz^2} + \nabla_t^2 + \frac{\omega^2}{c^2}\right) B_z^{\mathrm{TE}}(r, \theta, z, t)$$
$$= -\frac{4\pi}{c} \mathbf{e}_z \cdot (\nabla \times \mathbf{J}), \qquad (3)$$

$$\left(\frac{d^2}{dz^2} + \nabla_t^2 + \frac{\omega^2}{c^2}\right) E_z^{\mathrm{TM}}(r, \theta, z, t)$$
$$= 4\pi \frac{\partial \rho}{\partial z} + \frac{4\pi}{c^2} \frac{\partial J_z}{\partial t}. \qquad (4)$$

In Eqs. (3) and (4), $\nabla_t = \mathbf{e}_x \partial/\partial x + \mathbf{e}_y \partial/\partial y$, $\omega = 2\pi f$ is the (angular) frequency of the perturbations, $\mathbf{E}(\mathbf{x}, t)$ and $\mathbf{B}(\mathbf{x}, t)$, and the current and charge density perturbations are defined by

$$\mathbf{J}(\mathbf{x}, t) = -e \int \mathbf{v} f_1(\mathbf{x}, \mathbf{p}, t) d\mathbf{p}, \qquad (5)$$

$$\rho(\mathbf{x}, t) = -e \int f_1(\mathbf{x}, \mathbf{p}, t) d\mathbf{p}, \qquad (6)$$

where

$$f_1(\mathbf{x}, \mathbf{p}, t) = f(\mathbf{x}, \mathbf{p}, t) - f_0(r_g, p_\perp, p_z) \qquad (7)$$

is the distribution function perturbation, and $f_0(r_g, p_\perp, p_z)$ is the equilibrium distribution function. Note that the electron guiding-center radius and azimuthal angle, r_g and θ_g, and perpendicular and axial momentum components, $p_\perp = (p_x^2 + p_y^2)^{1/2}$ and p_z, are exact constants of motion for an individual electron in the applied magnetic field $B_0 \mathbf{e}_z$ (Fig. 2).
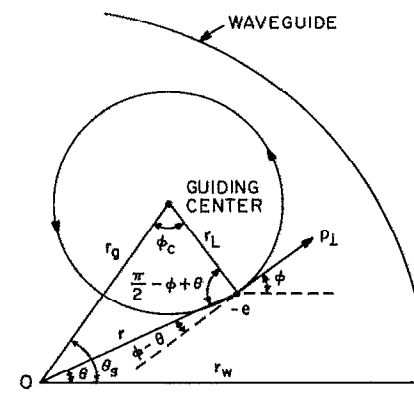

FIG. 1. Schematic of a CARM system in the interaction region.

FIG. 2. Guiding-center coordinate system.

Expanding $B_z^{\mathrm{TE}}(r,\theta,z)$ and $E_z^{\mathrm{TM}}(r,\theta,z)$ in terms of the vacuum TE_{mn} and TM_{mn} eigenfunctions $\Psi_{mn}(r,\theta)$ and $\widetilde{\Psi}_{mn}(r,\theta)$, respectively, the electromagnetic perturbations can be expressed in the general form

$$\mathbf{E}_t(\mathbf{x},t) = \frac{1}{2}\sum_{mn}\left(E_{mn}(z)\mathbf{e}_z\times\nabla_t\Psi_{mn}(r,\theta)\right.$$

$$\left. + \frac{c}{\omega}\frac{dB_{mn}(z)}{dz}\nabla_t\widetilde{\Psi}_{mn}(r,\theta)\right)$$

$$\times\exp(-i\omega t) + \text{c.c.}, \qquad (8)$$

$$E_z(\mathbf{x},t) = \frac{1}{2}\sum_{mn}\frac{c\tilde{k}_{mn}^2}{\omega}B_{mn}(z)\widetilde{\Psi}_{mn}(r,\theta)$$

$$\times\exp(-i\omega t) + \text{c.c.}, \qquad (9)$$

$$\mathbf{B}_t(\mathbf{x},t) = \frac{1}{2}\sum_{mn}\left(\frac{ic}{\omega}\frac{dE_{mn}(z)}{dz}\nabla_t\Psi_{mn}(r,\theta)\right.$$

$$\left. + iB_{mn}(z)\mathbf{e}_z\times\nabla_t\widetilde{\Psi}_{mn}(r,\theta)\right)$$

$$\times\exp(-i\omega t) + \text{c.c.}, \qquad (10)$$

$$B_z(\mathbf{x},t) = \frac{1}{2}\sum_{mn}\frac{ick_{mn}^2}{\omega}E_{mn}(z)\Psi_{mn}(r,\theta)$$

$$\times\exp(-i\omega t) + \text{c.c.} \qquad (11)$$

In Eqs. (8)–(11), the subscript t denotes the transverse components of the electromagnetic perturbations, and $E_{mn}(z)$ and $B_{mn}(z)$ are the z-dependent amplitude of the TE_{mn} and TM_{mn} modes, which evolve due to the CARM interaction. The TE_{mn} and TM_{mn} eigenfunctions

$$\Psi_{mn}(r,\theta) = C_{mn}J_m(k_{mn}r)\exp(im\theta), \qquad (12a)$$

$$\widetilde{\Psi}_{mn}(r,\theta) = \widetilde{C}_{mn}J_m(\tilde{k}_{mn}r)\exp(im\theta) \qquad (12b)$$

satisfy the equations

$$(\nabla_t^2 + k_{mn}^2)\Psi_{mn}(r,\theta) = 0, \qquad (13a)$$

$$(\nabla_t^2 + \tilde{k}_{mn}^2)\widetilde{\Psi}_{mn}(r,\theta) = 0, \qquad (13b)$$

and the boundary conditions

$$\frac{\partial\Psi_{mn}}{\partial r}(r = r_w,\theta) = 0, \qquad (14a)$$

$$\widetilde{\Psi}_{mn}(r = r_w,\theta) = 0. \qquad (14b)$$

Here, $J_m(x)$ is the Bessel function of first kind of order m, $v_{mn} = k_{mn}r_w$ is the nth zero of $J_m'(x) = dJ_m(x)/dx$, and $\tilde{v}_{mn} = \tilde{k}_{mn}r_w$ is the nth zero of $J_m(x)$. With the choice of the normalization factors

$$C_{mn}^2 = k_{mn}^2/\pi(v_{mn}^2 - m^2)J_m^2(v_{mn}), \qquad (15a)$$

$$\widetilde{C}_{mn}^2 = \tilde{k}_{mn}^2/\pi\tilde{v}_{mn}^2 J_m'^2(\tilde{v}_{mn}), \qquad (15b)$$

the orthogonality conditions can be expressed as

$$\int_{\pi r_w^2}\Psi_{mn}^*\Psi_{m'n'}\,d\sigma = \delta_{mm'}\delta_{nn'}, \qquad (16a)$$

$$\int_{\pi r_w^2}\widetilde{\Psi}_{mn}^*\widetilde{\Psi}_{m'n'}\,d\sigma = \delta_{mm'}\delta_{nn'}, \qquad (16b)$$

$$\int_{\pi r_w^2}\Psi_{mn}^*\widetilde{\Psi}_{m'n'}\,d\sigma = 0. \qquad (16c)$$

Here, δ_{mn} is the Kronecker delta. Substituting Eq. (11) into Eq. (3), multiplying the equation with Ψ_{mn}^*, and then integrating the equation over the cross section of the waveguide yields

$$\left(\frac{d^2}{dz^2} - k_{mn}^2 + \frac{\omega^2}{c^2}\right)E_{mn}(z)$$

$$= \frac{8\pi ie\omega\exp(i\omega t)}{c^2 k_{mn}^2}\int(\mathbf{e}_z\times\nabla_t\Psi_{mn}^*)\cdot\mathbf{v}f_1\,d\mathbf{p}\,d\sigma, \qquad (17)$$

for the TE_{mn} mode. Similarly, it is readily shown from Eqs. (4) and (9) that

$$\left(\frac{d^2}{dz^2} - \tilde{k}_{mn}^2 + \frac{\omega^2}{c^2}\right)B_{mn}(z)$$

$$= \frac{8\pi ie\omega^2\exp(i\omega t)}{c^2\tilde{k}_{mn}^2}\int\widetilde{\Psi}_{mn}^*\left(\frac{v_z}{c} + \frac{ic}{\omega}\frac{\partial}{\partial z}\right)f_1\,d\mathbf{p}\,d\sigma, \qquad (18)$$

for the TM_{mn} mode. The (average) rf power flow through the waveguide cross section as a function of interaction length, z, is given by

$$P(z) = \frac{c\omega}{8\pi^2}\int_0^{2\pi/\omega}dt\int(\mathbf{E}\times\mathbf{B})\cdot d\sigma. \qquad (19)$$

Substituting Eqs. (8)–(11) into Eq. (19) and making use of the orthogonality conditions in Eq. (16), we have

$$P(z) = \sum_{mn}\left[P_{mn}(z) + \widetilde{P}_{mn}(z)\right], \qquad (20)$$

where

$$P_{mn}(z) = \frac{ic^2 k_{mn}^2}{16\pi\omega}\left(E_{mn}\frac{dE_{mn}^*}{dz} - E_{mn}^*\frac{dE_{mn}}{dz}\right) \qquad (21)$$

and

$$\widetilde{P}_{mn}(z) = \frac{ic^2\tilde{k}_{mn}^2}{16\pi\omega}\left(B_{mn}\frac{dB_{mn}^*}{dz} - B_{mn}^*\frac{dB_{mn}}{dz}\right) \qquad (22)$$

are the rf powers in the TE_{mn} and TM_{mn} modes, respectively. In Secs. III and IV, use is made of Eqs. (1), (2), (17), and (18) to establish a linear and nonlinear theory of the multimode CARM interaction.

III. LINEAR THEORY

In this section, the Maxwell–Vlasov equations are linearized to derive self-consistent amplitude equations [Eqs. (40) and (41)] in the small-signal regime. The amplitude equations are solved with the Laplace transform technique, resulting in a dispersion relation [Eqs. (44) and (45)] for the CARM instability which includes an arbitrary number of TE and TM waveguide modes. Our Laplace transform analysis allows for analytical calculation of launching losses and the three-dimensional radiation field profile.

A. The linearized Vlasov equation

For present purposes, we assume the electron beam to be cold and azimuthally symmetric with respect to the waveguide axis, and express the equilibrium distribution function as

$$f_0(r_g,p_\perp,p_z) = \frac{n_b}{2\pi p_{\perp 0}}\delta(p_\perp - p_{\perp 0})\delta(p_z - p_{z0})G(r_g),$$
(23)

where n_b is the number of electrons per unit axial length, and

$$\int G(r_g)r_g\,dr_g\,d\theta_g = 1.$$
(24)

The electron phase-space density perturbation $f_1(\mathbf{x},\mathbf{p},t)$ evolves according to the linearized Vlasov equation

$$v_z\frac{df_1}{dz} \equiv \frac{\partial f_1}{\partial t} + \mathbf{v}\cdot\frac{\partial f_1}{\partial \mathbf{x}} - \frac{e}{c}(\mathbf{v}\times B_0\mathbf{e}_z)\cdot\frac{\partial f_1}{\partial \mathbf{p}}$$

$$= e\left(\mathbf{E} + \frac{\mathbf{v}}{c}\times\mathbf{B}\right)\cdot\frac{\partial f_0}{\partial \mathbf{p}}.$$
(25)

Here, since the system is single frequency and the spatial evolution of the perturbations is of interest, the usual total time derivative is replaced by total derivative with respect to the axial distance z. It is convenient to introduce guiding-center variables as illustrated in Fig. 2, where $r_L = p_\perp/m_0\Omega_c$ is the Larmor radius, $p_x = p_\perp\cos\phi$, $p_y = p_\perp\sin\phi$, $\mathbf{e}_\perp = \mathbf{e}_r\cos(\phi-\theta) + \mathbf{e}_\theta\sin(\phi-\theta)$, and $\mathbf{e}_\phi = -\mathbf{e}_r\times\sin(\phi-\theta) + \mathbf{e}_\theta\cos(\phi-\theta)$. Using

$$\frac{\partial f_0}{\partial \mathbf{p}} = \mathbf{e}_\perp\left(\frac{\partial f_0}{\partial p_\perp} + \frac{\cos\phi_c}{m_0\Omega_c}\frac{\partial f_0}{\partial r_g}\right) - \mathbf{e}_\phi\frac{\sin\phi_c}{m_0\Omega_c}\frac{\partial f_0}{\partial r_g} + \mathbf{e}_z\frac{\partial f_0}{\partial p_z},$$
(26)

Eq. (25) becomes

$$v_z\frac{d}{dz}f_1(r,\theta,z,p_\perp,\phi,p_z,t)$$

$$= e(E_\perp - \beta_z B_\phi)\frac{\partial f_0}{\partial p_\perp} + e(E_z + \beta_\perp B_\phi)\frac{\partial f_0}{\partial p_z}$$

$$+ (e/m_0\Omega_c)[(E_\perp\cos\phi_c - E_\phi\sin\phi_c)$$

$$- \beta_z(B_\perp\sin\phi_c + B_\phi\cos\phi_c) + \beta_\perp B_z\sin\phi_c]\frac{\partial f_0}{\partial r_g},$$
(27)

where $\beta_\perp = v_\perp/c$ and $\beta_z = v_z/c$. Substituting Eqs. (8)–(11) into Eq. (27) and making use of recurrence relations and Graf's theorem for Bessel functions,[27] it can be shown (see Appendix A) that the linearized Vlasov equation can be expressed as

$$\frac{df_1}{dz} = \frac{e}{2v_z}\sum_{mn}\sum_{q=-\infty}^{\infty}(k_{mn}C_{mn}O_{mnq} + \tilde{k}_{mn}\tilde{C}_{mn}\tilde{O}_{mnq})f_0$$

$$\times\exp[i\Lambda_{mq}(\phi,\phi_c,t)] + \text{c.c.},$$
(28)

where $\Lambda_{mq}(\phi,\phi_c,t) = m\phi + q\phi_c - \omega t - m\pi/2$, and the operators O_{mnq} and $\tilde{O}_{mnq}$ are defined by

$$O_{mnq}\left(z,r_g,r_L,\frac{\partial}{\partial r_g},p_\perp,p_z,\frac{\partial}{\partial p_\perp},\frac{\partial}{\partial p_z}\right)$$

$$= X_{mnq}(r_L,r_g)\left[\left(E_{mn} + \frac{iv_z}{\omega}\frac{dE_{mn}}{dz}\right)\frac{\partial}{\partial p_\perp}\right.$$

$$\left. - \frac{iv_\perp}{\omega}\frac{dE_{mn}}{dz}\frac{\partial}{\partial p_z}\right]$$

$$- \left[\frac{Y_{mnq}(r_L,r_g)}{m_0\Omega_c}\left(E_{mn} + \frac{iv_z}{\omega}\frac{dE_{mn}}{dz}\right)\right.$$

$$\left. - \frac{Z_{mnq}(r_L,r_g)}{m_0\Omega_c}\left(\frac{k_{mn}v_\perp}{2\omega}\right)E_{mn}\right]\frac{\partial}{\partial r_g},$$
(29)

$$\tilde{O}_{mnq}\left(z,r_g,r_L,\frac{\partial}{\partial r_g},p_\perp,p_z,\frac{\partial}{\partial p_\perp},\frac{\partial}{\partial p_z}\right)$$

$$= \tilde{X}_{mnq}(r_L,r_g)\left[\left(\beta_z B_{mn} + \frac{ic}{\omega}\frac{dB_{mn}}{dz}\right)\frac{\partial}{\partial p_\perp}\right.$$

$$\left. - \left(\beta_\perp - \frac{c\tilde{k}_{mn}^2 r_L}{(m+q)\omega}\right)B_{mn}\frac{\partial}{\partial p_z}\right]$$

$$+ \frac{\tilde{Y}_{mnq}(r_L,r_g)}{m_0\Omega_c}\left(\beta_z B_{mn} + \frac{ic}{\omega}\frac{dB_{mn}}{dz}\right)\frac{\partial}{\partial r_g}.$$
(30)

In Eqs. (29) and (30), the geometric factors X, Y, Z, $\tilde{X}$, and $\tilde{Y}$ are defined by

$$X_{mnq}(r_L,r_g) = J'_{m+q}(k_{mn}r_L)J_q(k_{mn}r_g),$$
(31)

$$Y_{mnq}(r_L,r_g) = J_{m+q}(k_{mn}r_L)J'_q(k_{mn}r_g),$$
(32)

$$Z_{mnq}(r_L,r_g) = J_{m+q-1}(k_{mn}r_L)J_{q-1}(k_{mn}r_g)$$

$$- J_{m+q+1}(k_{mn}r_L)J_{q+1}(k_{mn}r_g),$$
(33)

$$\tilde{X}_{mnq}(r_L,r_g) = (m+q)[J_{m+q}(\tilde{k}_{mn}r_L)/\tilde{k}_{mn}r_L]$$

$$\times J_q(\tilde{k}_{mn}r_g),$$
(34)

$$\tilde{Y}_{mnq}(r_L,r_g) = qJ_{m+q}(\tilde{k}_{mn}r_L)[J_q(\tilde{k}_{mn}r_g)/\tilde{k}_{mn}r_g].$$
(35)

Integrating Eq. (28) along the line of characteristics defined by

$$\phi_c(z') = \phi_c + (\Omega_c/\gamma v_z)(z' - z),$$
(36a)

$$\phi(z') = \phi + (\Omega_c/\gamma v_z)(z' - z),$$
(36b)

$$t(z') = t + (1/v_z)(z' - z),$$
(36c)

yields

$$f_1(r_g,\phi_c,z,p_\perp,\phi,p_z,t)$$

$$= \frac{e}{2}\sum_{mnq}\exp[i\Lambda_{mq}(\phi,\phi_c,t)]\int_0^z\frac{dz'}{v_z}$$

$$\times\exp\{i[(m+q)(\Omega_c/\gamma) - \omega][(z'-z)/v_z]\}$$

$$\times[k_{mn}C_{mn}O_{mnq}(z') + \tilde{k}_{mn}\tilde{C}_{mn}\tilde{O}_{mnq}(z')]f_0 + \text{c.c.}$$
(37)

In deriving Eq. (37), we have assumed the initial condition $f_1|_{z=0} = 0$, corresponding to an initially unbunched electron beam. In Eq. (37), use has been made of the abbreviations $O_{mnq}(z') = O_{mnq}(z',r_g,r_L,\partial/\partial r_g,p_\perp,p_z,\partial/\partial p_\perp,\partial/\partial p_z)$ and $\tilde{O}_{mnq}(z') = O_{mnq}(z',r_g,r_L,\partial/\partial r_g,p_\perp,p_z,\partial/\partial p_\perp,\partial/\partial p_z)$, and the variables (r,θ,z) in f_1 have been replaced by the guiding-center variables (r_g,ϕ_c,z) via a scalar transformation.

B. Linearized amplitude equations for coupled TE and TM modes

To evaluate the overlap integrals in Eqs. (17) and (18), we express $\boldsymbol{\beta}\cdot(\mathbf{e}_z\times\nabla\Psi^*_{mn})\exp(i\omega t)$ and $\tilde{\Psi}^*_{mn}\exp(i\omega t)$ in terms of guiding-center variables, i.e.,

$$\boldsymbol{\beta} \cdot (\mathbf{e}_z \times \nabla \Psi_{mn}^*) \exp(i\omega t)$$

$$= \beta_\perp k_{mn} C_{mn} \sum_q X_{mnq}(r_L, r_g) \exp[-i\Lambda_{mq}(\phi, \phi_c, t)], \tag{38}$$

$$\widetilde{\Psi}_{mn}^* \exp(i\omega t)$$

$$= \widetilde{C}_{mn} \sum_q \frac{\widetilde{k}_{mn} r_L}{(m+q)} \widetilde{X}_{mnq}(r_L, r_g)$$

$$\times \exp[-i\Lambda_{mq}(\phi, \phi_c, t)]. \tag{39}$$

Substituting Eqs. (37)–(39) into Eqs. (17) and (18) and making use of the expressions $d\sigma = r \, dr \, d\theta = r_g \, dr_g \, d\phi_c$ and $d\mathbf{p} = p_\perp \, dp_\perp \, dp_z \, d\phi$ result in the linearized amplitude equations

$$\left(\frac{d^2}{dz^2} - k_{mn}^2 + \frac{\omega^2}{c^2}\right) E_{mn}(z)$$

$$= i \frac{16\pi^3 e^2 \omega}{c} \left(\frac{C_{mn}}{k_{mn}}\right) \sum_{n'} \sum_{l=-\infty}^{\infty} \int r_g \, dr_g$$

$$\times X_{mnl-m}(r_L, r_g) \int p_\perp \, dp_\perp \, dp_z \, \beta_\perp$$

$$\times \int_0^z \frac{dz'}{v_z} \exp\left[i\left(l\frac{\Omega_c}{\gamma} - \omega\right)\frac{(z'-z)}{v_z}\right]$$

$$\times [k_{mn'} C_{mn'} O_{mn'l-m}(z')$$

$$+ \widetilde{k}_{mn'} \widetilde{C}_{mn'} \widetilde{O}_{mn'l-m}(z')] f_0 \tag{40}$$

and

$$\left(\frac{d^2}{dz^2} - \widetilde{k}_{mn}^2 + \frac{\omega^2}{c^2}\right) B_{mn}(z)$$

$$= i \frac{16\pi^3 e^2 \omega^2}{c^2 \widetilde{k}_{mn}} \left(\frac{\widetilde{C}_{mn}}{\widetilde{k}_{mn}}\right) \sum_{n'} \sum_{l=-\infty}^{\infty} \int r_g \, dr_g \frac{\widetilde{k}_{mn} r_L}{l}$$

$$\times \widetilde{X}_{mnl-m}(r_L, r_g) \int p_\perp \, dp_\perp \, dp_z \left(\beta_z + \frac{ic}{\omega}\frac{\partial}{\partial z}\right)$$

$$\times \int_0^z \frac{dz'}{v_z} \exp\left[i\left(l\frac{\Omega_c}{\gamma} - \omega\right)\frac{(z'-z)}{v_z}\right]$$

$$\times [k_{mn'} C_{mn'} O_{mn'l-m}(z')$$

$$+ \widetilde{k}_{mn'} \widetilde{C}_{mn'} \widetilde{O}_{mn'l-m}(z')] f_0. \tag{41}$$

Equations (40) and (41) describe the linear evolution of coupled TE and TM waveguide modes in a CARM amplifier for an (arbitrary) azimuthally symmetric electron beam. Note in Eqs. (40) and (41) that TE and/or TM modes with different azimuthal numbers do not couple, which is a direct consequence of the assumption made of the azimuthal symmetry of the electron beam with $\partial/\partial\theta_g = 0$. [For an asymmetric electron beam ($\partial/\partial\theta_g \neq 0$), of course, the coupling of modes with different azimuthal numbers cannot be excluded.]

C. Dispersion relation and launching losses

To derive a dispersion relation for the CARM instability with TE and TM modes and to calculate launching losses, we solve Eqs. (40) and (41) with the Laplace transform defined by

$$\widetilde{E}_{mn}(s) = \int_0^\infty E_{mn}(z) \exp(-sz) dz, \tag{42}$$

$$\widetilde{B}_{mn}(s) = \int_0^\infty B_{mn}(z) \exp(-sz) dz. \tag{43}$$

A detailed derivation of the resulting dispersion relation is presented in Appendix B for the case of a thin ($k_{mn} r_g \ll 1$ and $\widetilde{k}_{mn} r_g \ll 1$) electron beam described by the equilibrium distribution function in Eq. (23). For the initial conditions

$$E_{mn}|_{z=0} = E_{mn}(0), \quad B_{mn}|_{z=0} = B_{mn}(0),$$

$$\left.\frac{dE_{mn}}{dz}\right|_{z=0} = \left.\frac{dB_{mn}}{dz}\right|_{z=0} = 0,$$

the dispersion relation can be expressed in the matrix form

$$D_{mn}^{TE}(s,\omega) \widetilde{E}_{mn}(s) + \sum_{n'(n'\neq n)} \sum_{l=-\infty}^{\infty} \epsilon_{mnn'l}^{TE} \frac{k_{mn'}^2(\omega^2 + c^2 s^2)}{(\omega - l\Omega_c/\gamma + isv_z)^2} \widetilde{E}_{mn'}(s)$$

$$+ \sum_{n'} \sum_{l=-\infty}^{\infty} \epsilon_{mnn'l}^{EM} \frac{(c^2 \widetilde{k}_{mn'}^4 \gamma\omega/l\Omega_c^2)(\beta_z\omega + ics)}{(\omega - l\Omega_c/\gamma + isv_z)^2} \widetilde{B}_{mn'}(s)$$

$$= sE_{mn}(0) + \sum_{n'} \sum_{l=-\infty}^{\infty} \left(\epsilon_{mnn'l}^{TE} \frac{iv_z k_{mn'}^2 \omega}{(\omega - l\Omega_c/\gamma + isv_z)^2} E_{mn'}(0) + \epsilon_{mnn'l}^{EM} \frac{ic\widetilde{k}_{mn'}^2 \omega}{(\omega - l\Omega_c/\gamma + isv_z)^2} B_{mn'}(0)\right), \tag{44}$$

$$D_{mn}^{TM}(s,\omega) \widetilde{B}_{mn}(s) + \sum_{n'(n'\neq n)} \sum_{l=-\infty}^{\infty} \epsilon_{mnn'l}^{ME} \frac{(k_{mn'}^2 \gamma/l\Omega_c)(\beta_z\omega + ics)(\omega^2 + c^2 s^2)}{(\omega - l\Omega_c/\gamma + isv_z)^2} \widetilde{E}_{mn'}(s)$$

$$+ \sum_{n'} \sum_{l=-\infty}^{\infty} \epsilon_{mnn'l}^{TM} \frac{l(c\widetilde{k}_{mn'}^2 \gamma/l\Omega_c)^2(\beta_z\omega + ics)^2}{(\omega - l\Omega_c/\gamma + isv_z)^2} \widetilde{B}_{mn'}(s)$$

$$= sB_{mn}(0) + \sum_{n'} \sum_{l=-\infty}^{\infty} \left(\epsilon_{mnn'l}^{ME} \frac{(c^2 k_{mn'}^2 \gamma/l\Omega_c)(\beta_z\omega + ics)s}{(\omega - l\Omega_c/\gamma + isv_z)^2} E_{mn'}(0)\right)$$

$$+ \epsilon_{mnn'l}^{TM} \frac{i(c\widetilde{k}_{mn'}^3 \gamma\omega/l\Omega_c\widetilde{k}_{mn})(\beta_z\omega + ics)}{(\omega - l\Omega_c/\gamma + isv_z)^2} B_{mn'}(0)\right), \tag{45}$$

where

$$D_{mn}^{TE}(s,\omega) = s^2 - k_{mn}^2 + \frac{\omega^2}{c^2} + \sum_{l=-\infty}^{\infty} \epsilon_{mnnl}^{TE}$$

$$\times \frac{k_{mn}^2(\omega^2 + c^2s^2)}{(\omega - l\Omega_c/\gamma + isv_z)^2} \qquad (46)$$

is the dielectric function for the (single) TE_{mn} mode, and

$$D_{mn}^{TM}(s,\omega) = s^2 - \tilde{k}_{mn}^2 + \omega^2/c^2$$

$$+ \sum_{l=-\infty}^{\infty} \epsilon_{mnnl}^{TM} \frac{l(c\tilde{k}_{mn}^2\gamma/l\Omega_c)^2(\beta_z\omega + ics)^2}{(\omega - l\Omega_c/\gamma + isv_z)^2} \qquad (47)$$

for the (single) TM_{mn} mode. In Eqs. (44)–(47),

$$\epsilon_{mnn'l}^{TE} = \alpha(C_{mn}/k_{mn})(C_{mn'}/k_{mn'})X_{mnl-m}(r_L,r_g)$$

$$\times X_{mn'l-m}(r_L,r_g), \qquad (48)$$

$$\epsilon_{mnn'l}^{EM} = \alpha(C_{mn}/k_{mn})(\tilde{C}_{mn'}/\tilde{k}_{mn'})X_{mnl-m}(r_L,r_g)$$

$$\times \tilde{X}_{mn'l-m}(r_L,r_g), \qquad (49)$$

$$\epsilon_{mnn'l}^{TM} = \alpha(\tilde{C}_{mn}/\tilde{k}_{mn})(\tilde{C}_{mn'}/\tilde{k}_{mn'})\tilde{X}_{mnl-m}(r_L,r_g)$$

$$\times \tilde{X}_{mn'l-m}(r_L,r_g), \qquad (50)$$

$$\epsilon_{mnn'l}^{ME} = \alpha(\tilde{C}_{mn}/\tilde{k}_{mn})(C_{mn'}/k_{mn'})\tilde{X}_{mnl-m}(r_L,r_g)$$

$$\times X_{mn'l-m}(r_L,r_g) \qquad (51)$$

are dimensionless coupling constants. Here,

$$\alpha = \frac{4\pi e^2 n_b \beta_\perp^2}{\gamma m_0 c^2} = \frac{4\pi\beta_\perp^2}{\gamma\beta_z}\left(\frac{I_b}{I_A}\right), \qquad (52)$$

$I_b = 2\pi e n_b \beta_z c \int_0^{r_m} G(r_g)r_g\,dr_g$ is the beam current, r_m is the maximum guiding-center radius of the beam electrons, and $I_A = m_0 c^3/e \cong 17$ kA is the Alfvén current. In Eqs. (44)–(47), we have kept only the terms of order $c^2 k_{mn}^2/(\omega - l\Omega_c/\gamma + isv_z)^2$, and neglected terms of order $ck_{mn}/(\omega - l\Omega_c/\gamma + isv_z)$, etc. [More exact relations corresponding to Eqs. (44)–(47) which include the contributions of order $ck_{mn}/(\omega - l\Omega_c/\gamma + isv_z)$ can be obtained from Eqs. (B5)–(B12) in Appendix B.]

To leading order in $c^2 k_{mn}^2/(\omega - l\Omega_c/\gamma - kv_z)^2$, our results in Eqs. (44) and (45) have the same form as Eq. (66) in Ref. 7. The coupling constants are evaluated for a thin solid electron beam, while an annular beam is considered in Ref. 7. The exact coupling constants are defined in Eqs. (B5)–(B12) in Appendix B, and can be evaluated for an arbitrary azimuthally symmetric electron beam, including an annular beam profile.

The dispersion relation for the multimode CARM interaction is given by the zero determinant of the coefficient matrix on the left-hand side of Eqs. (44) and (45). Moreover, the amplitudes $\tilde{E}_{mn}(s)$ and $\tilde{B}_{mn}(s)$ are easily found by solving the linear algebraic equations (44) and (45), and $E_{mn}(z)$ and $B_{mn}(z)$ can be obtained by performing the inverse Laplace transform of $\tilde{E}_{mn}(s)$ and $\tilde{B}_{mn}(s)$,

$$E_{mn}(z) = \frac{1}{2\pi i}\int_{\sigma-i\infty}^{\sigma+i\infty} \tilde{E}_{mn}(s)\exp(sz)ds, \qquad (53)$$

$$B_{mn}(z) = \frac{1}{2\pi i}\int_{\sigma-i\infty}^{\sigma+i\infty} \tilde{B}_{mn}(s)\exp(sz)ds. \qquad (54)$$

IV. NONLINEAR THEORY

We now present a fully nonlinear, three-dimensional, self-consistent theory of an overmoded CARM amplifier for an (arbitrary) azimuthally symmetric electron beam. The present nonlinear model is capable of dealing with a single TE or TM mode, multiple TE and/or TM modes, cyclotron harmonics, magnetic field tapering, momentum and energy spread, etc.

A. Particle dynamics

Following Fliflet's treatment[12] of the single-mode CARM interaction, we assume that the electron guiding-center radius and angle are approximate constants of motion, i.e.,

$$\frac{dr_g}{dt} \cong 0 \quad \text{and} \quad \frac{d\theta_g}{dt} \cong 0. \qquad (55)$$

In addition, we introduce the notation (the Larmor radius)

$$r_L = p_\perp/m_0\Omega_c, \qquad (56)$$

where $p_\perp = [(\gamma^2-1)m_0^2c^2 - p_z^2]^{1/2}$. Under these assumptions, the motion of an electron can be described by three variables: the energy, $\gamma m_0 c^2$, the axial momentum, p_z, and the azimuthal angle, $\phi = \tan^{-1}(p_y/p_x)$. From the Lorentz force equation (1), the dynamics of each individual electron is then

$$\frac{d\gamma}{dt} = -\frac{e}{\gamma m_0^2 c^2}(p_\perp E_\perp + p_z E_z), \qquad (57)$$

$$\frac{dp_z}{dt} = -e\left(E_z + \frac{p_\perp B_\phi}{\gamma m_0 c}\right), \qquad (58)$$

$$\frac{d\phi}{dt} = \frac{\Omega_c}{\gamma} - \frac{e}{p_\perp}\left(E_\phi + \frac{p_z B_\perp}{\gamma m_0 c} - \frac{p_\perp B_z}{\gamma m_0 c}\right). \qquad (59)$$

It is useful to introduce the dimensionless wave amplitudes, $A_{mn}(z)$ and $\tilde{A}_{mn}(z)$, and phase shifts, $\delta_{mn}(z)$ and $\tilde{\delta}_{mn}(z)$, for the TE_{mn} and TM_{mn} modes, so that

$$E_{mn}(z) = \left(\frac{k_{mn}}{C_{mn}}\right)\left(\frac{\omega}{ck_{mn}}\right)^2\left(\frac{I_A}{\omega}\right)A_{mn}(z)$$

$$\times \exp\{i[k_{zmn}z + \delta_{mn}(z)]\}, \qquad (60)$$

$$B_{mn}(z) = \left(\frac{\tilde{k}_{mn}}{\tilde{C}_{mn}}\right)\left(\frac{\omega}{c\tilde{k}_{mn}}\right)^2\left(\frac{I_A}{\omega}\right)\tilde{A}_{mn}(z)$$

$$\times \exp\{i[\tilde{k}_{zmn}z + \tilde{\delta}_{mn}(z)]\}. \qquad (61)$$

Symbol δ is used hereinafter to represent the phase shift [instead of the Kronecker delta used in Eq. (16)]. The axial wave numbers of the vacuum TE_{mn} and TM_{mn} waveguide modes, k_{zmn} and $\tilde{k}_{zmn}$, are defined by

$$\omega^2 = c^2(k_{zmn}^2 + k_{mn}^2) \qquad (62a)$$

and

$$\omega^2 = c^2(\bar{k}_{zmn}^2 + \bar{k}_{mn}^2), \tag{62b}$$

respectively.

Substituting Eqs. (8)–(11) into Eqs. (57)–(59) and making use of Graf's theorem for Bessel functions (similar to Appendix A), it can be shown after some straightforward algebra that the normalized equations of motion for an electron are

$$\frac{d\gamma}{d\hat{z}} = -\frac{\hat{p}_\perp}{\hat{p}_z} \sum_{mnl} X_{mnl-m}(r_g, r_L) A_{mn} \cos\psi_{mnl}$$
$$-\frac{\hat{p}_\perp}{\hat{p}_z} \sum_{mnl} \widetilde{X}_{mnl-m}(r_g, r_L) \left[\left((\beta_{z0} - \bar{\beta}_{\phi mn}^{-1}) \frac{\gamma_0}{l\hat{\Omega}_c} \right.\right.$$
$$\left.\left. - \frac{d\tilde{\delta}_{mn}}{d\hat{z}} \right) \widetilde{A}_{mn} \cos\tilde{\psi}_{mnl} - \frac{d\widetilde{A}_{mn}}{d\hat{z}} \sin\tilde{\psi}_{mnl} \right], \tag{63}$$

$$\frac{d\hat{p}_z}{d\hat{z}} = -\frac{\hat{p}_\perp}{\hat{p}_z} \sum_{mnl} X_{mnl-m}$$
$$\times \left[\left(\beta_{\phi mn}^{-1} + \frac{d\delta_{mn}}{d\hat{z}} \right) A_{mn} \cos\psi_{mnl} \right.$$
$$\left. + \frac{dA_{mn}}{d\hat{z}} \sin\psi_{mnl} \right] - \frac{\hat{p}_\perp}{\hat{p}_z} \sum_{mnl} \widetilde{X}_{mnl-m} \left(\frac{\gamma_0 \widehat{\tilde{\omega}}_{cmn}^2}{l\hat{\Omega}_c} - 1 \right)$$
$$\times \widetilde{A}_{mn} \cos\tilde{\psi}_{mnl}, \tag{64}$$

$$\frac{d\phi}{d\hat{z}} = \frac{\hat{\Omega}_c}{\hat{p}_z} + \frac{1}{\hat{p}_z\hat{p}_\perp} \sum_{mnl} W_{mnl-m} \left\{ \left[\gamma - \hat{p}_z \left(\beta_{\phi mn}^{-1} + \frac{d\delta_{mn}}{d\hat{z}} \right) \right] \right.$$
$$\left. \times A_{mn} \sin\psi_{mnl} + \hat{p}_z \frac{dA_{mn}}{d\hat{z}} \cos\psi_{mnl} \right\} + \frac{1}{\hat{p}_z\hat{p}_\perp}$$
$$\times \sum_{mnl} \widetilde{W}_{mnl-m} \left\{ \left[\hat{p}_z - \gamma \left(\bar{\beta}_{\phi mn}^{-1} + \frac{d\tilde{\delta}_{mn}}{d\hat{z}} \right) \right] \widetilde{A}_{mn} \right.$$
$$\left. \times \sin\tilde{\psi}_{mnl} + \gamma \frac{d\widetilde{A}_{mn}}{d\hat{z}} \cos\tilde{\psi}_{mnl} \right\}. \tag{65}$$

In Eqs. (63)–(65), the (ponderomotive) phase variables, ψ_{mnl} and $\tilde{\psi}_{mnl}$, are related to the phase ϕ by the

$$\psi_{mnl} = k_{zmn}z + \delta_{mn}(z)$$
$$+ l\phi - \omega t - (l-m)\theta_g + (l-2m)\pi/2, \tag{66}$$
$$\tilde{\psi}_{mnl} = \bar{k}_{zmn}z + \tilde{\delta}_{mn}(z)$$
$$+ l\phi - \omega t - (l-m)\theta_g + (l-2m)\pi/2. \tag{67}$$

The normalized variables and parameters are defined by

$$\hat{p}_z = \frac{p_z}{m_0 c}, \quad \hat{p}_\perp = \frac{p_\perp}{m_0 c}, \quad \hat{z} = \frac{\omega z}{c},$$
$$\widehat{\omega}_{cmn} = \frac{\omega_{cmn}}{\omega} = \frac{ck_{mn}}{\omega}, \quad \widehat{\tilde{\omega}}_{cmn} = \frac{\tilde{\omega}_{cmn}}{\omega} = \frac{c\bar{k}_{mn}}{\omega},$$
$$\tag{68}$$
$$\beta_{\phi mn} = \frac{\omega}{ck_{zmn}}, \quad \bar{\beta}_{\phi mn} = \frac{\omega}{c\bar{k}_{zmn}}, \quad \hat{\Omega}_c = \frac{\Omega_c}{\omega}.$$

The geometric factors X_{mnl-m} and $\widetilde{X}_{mnl-m}$ are defined in Eqs. (31) and (34), and

$$W_{mnl-m}(r_L, r_g) = l[J_l(k_{mn}r_L)/k_{mn}r_L]$$
$$\times J_{l-m}(k_{mn}r_g), \tag{69}$$

$$\widetilde{W}_{mnl-m}(r_L, r_g) = J_l'(\bar{k}_{mn}r_L)J_{l-m}(\bar{k}_{mn}r_g). \tag{70}$$

B. Wave equations

For an azimuthally symmetric electron beam, the nonlinear charge and current density perturbations can be expressed as[28]

$$\rho(\mathbf{x},t) = -en_b G(r_g)v_{z0} \int_{-\infty}^{\infty} \frac{m_0\gamma(t_0,t)}{p_z(t_0,t)}$$
$$\times \delta[t - \tau(t_0,z)]dt_0, \tag{71}$$

$$\mathbf{J}(\mathbf{x},t) = -en_b G(r_g)v_{z0} \int_{-\infty}^{\infty} \frac{\mathbf{p}(t_0,t)}{p_z(t_0,t)}$$
$$\times \delta[t - \tau(t_0,z)]dt_0, \tag{72}$$

where $\mathbf{p}(t_0,t)$ and $\gamma(t_0,t)m_0c^2$ are the instantaneous momentum and energy of an electron (at time t) which crossed the plane $z = 0$ at time t_0, and $\tau(t_0,z)$ is the time when this electron reaches the axial distance z. Substituting Eqs. (71) and (72) into Eqs. (17) and (18) and averaging over one period $2\pi/\omega$, the wave equations for the TE and TM modes can be expressed in the normalized form

$$\left(\frac{d^2}{d\hat{z}^2} + \beta_{\phi mn}^{-2} \right) A_{mn}(\hat{z}) \exp\left[i\left(\frac{\hat{z}}{\beta_{\phi mn}} + \delta_{mn}(\hat{z}) \right) \right]$$
$$= \frac{2ig_{mn}}{\beta_{\phi mn}} \left\langle X_{mnl-m}(r_g, r_L) \frac{\hat{p}_\perp}{\hat{p}_z} \exp(-i\psi_{mnl}) \right\rangle$$
$$\times \exp\{i[\hat{z}/\beta_{\phi mn} + \delta_{mn}(\hat{z})]\}, \tag{73}$$

$$\left(\frac{d^2}{d\hat{z}^2} + \bar{\beta}_{\phi mn}^{-2} \right) \widetilde{A}_{mn}(\hat{z}) \exp\left[i\left(\frac{\hat{z}}{\bar{\beta}_{\phi mn}} + \tilde{\delta}_{mn}(\hat{z}) \right) \right]$$
$$= \frac{2i\tilde{g}_{mn}}{\bar{\beta}_{\phi mn}} \left\langle \widetilde{X}_{mnl-m}(r_g, r_L) \frac{\hat{p}_\perp}{\hat{p}_z} \exp(-i\tilde{\psi}_{mnl}) \right\rangle$$
$$\times \exp\{i[\hat{z}/\bar{\beta}_{\phi mn} + \tilde{\delta}_{mn}(\hat{z})]\}, \tag{74}$$

where $\langle F \rangle = N^{-1}\Sigma_{i=1}^N F_i$ denotes the ensemble average over the particle distribution, N is the number of particles used in the simulations, and

$$g_{mn} = 4\pi\beta_{\phi mn} \left(\frac{ck_{mn}}{\omega} \right)^2 \left(\frac{C_{mn}}{k_{mn}} \right)^2 \left(\frac{I_b}{I_A} \right), \tag{75a}$$

$$\tilde{g}_{mn} = 4\pi\bar{\beta}_{\phi mn} \left(\frac{c\bar{k}_{mn}}{\omega} \right)^2 \left(\frac{\widetilde{C}_{mn}}{\bar{k}_{mn}} \right)^2$$
$$\times \left(\frac{\gamma_0}{l\hat{\Omega}_c} \right) \left(\beta_{z0} - \frac{1}{\bar{\beta}_{\phi mn}} \right) \left(\frac{I_b}{I_A} \right) \tag{75b}$$

are the normalized coupling constants for the TE_{mn} and TM_{mn} modes, respectively.

Substituting Eq. (60) into Eq. (21), and Eq. (61) into Eq. (22) yields the rf power associated with TE_{mn} and TM_{mn} modes

$$P_{mn}(\hat{z}) = \frac{1}{8\pi} \left(\frac{m_0^2 c^5}{e^2} \right) \left(\beta_{\phi mn}^{-1} + \frac{d\delta_{mn}}{d\hat{z}} \right)$$
$$\times \left(\frac{\omega}{ck_{mn}} \right)^2 \left(\frac{k_{mn}}{C_{mn}} \right)^2 A_{mn}^2, \tag{76}$$

$$\tilde{P}_{mn}(\hat{z}) = \frac{1}{8\pi}\left(\frac{m_0^2 c^5}{e^2}\right)\left(\tilde{\beta}_{\delta mn}^{-1} + \frac{d\tilde{\delta}_{mn}}{d\hat{z}}\right)$$

$$\times \left(\frac{\omega}{c\tilde{k}_{mn}}\right)^2 \left(\frac{\tilde{k}_{mn}}{\tilde{C}_{mn}}\right)^2 \tilde{A}_{mn}^2, \qquad (77)$$

where $m_0^2 c^5/e^2 \cong 8.7$ GW.

We have developed a three-dimensional simulation code, CSPOT, which solves the complete CARM amplifier equations (63)–(65), (73) and (74). For a simulation with N particles and M modes, the code integrates numerically a total of $3N + 2M$ first-order ordinary differential equations (typically, $N \geqslant 1024$). This code has been benchmarked against the linear theory presented in Sec. III, and can model a single TE or TM mode, multiple TE and/or TM modes, cyclotron harmonics, magnetic field tapering, momentum and energy spread, waveguide losses, and various beam loading options. After reviewing the single-mode CARM interaction (Sec. V), we use our linear and nonlinear theory to analyze CARM amplifiers with two or more waveguide modes, and illustrate the general features of multimode phenomena (Sec. VI).

V. NUMERICAL ANALYSIS FOR A SINGLE MODE

In this section, we review the stability properties of single-mode CARM interaction. Here, emphasis is placed on the analytical calculation of launching losses using the Laplace transform formalism, and on detailed comparisons between linear theory and results from computer simulations.

A. Single TE mode

As stated in the Introduction the CARM interaction occurs when the cyclotron resonance condition

$$\omega - l\Omega_c/\gamma - k_z v_z = 0 \qquad (78)$$

is approximately satisfied (Fig. 3). Here, $ik_z = s$, and l is the harmonic number. To leading order in $c^2 k_{mn}^2/(\omega - l\Omega_c/\gamma - k_z v_z)^2$, it follows from Eqs. (44) and (46) that the dispersion relation with the single TE_{mn} mode can be expressed as

$$D_{mn}^{TE}(ik_z,\omega) = \frac{\omega^2}{c^2} - k_z^2 - k_{mn}^2 + \epsilon_{mnnl}^{TE}$$

$$\times \frac{k_{mn}^2(\omega^2 - c^2 k_z^2)}{(\omega - l\Omega_c/\gamma - k_z v_z)^2} = 0, \qquad (79)$$

which is in agreement with earlier results.[12,22,29] The maximum spatial growth rate for the single TE_{mn} mode occurs when $\omega^2 - c^2(k_{mn}^2 + k_z^2) \cong 0$ and $\omega - l\Omega_c/\gamma - k_z v_z \cong 0$, corresponding to the intersection of the uncoupled TE_{mn} and beam cyclotron modes. Therefore, expanding $k_z = k_{zmn} + \delta k_z$ with $k_{zmn} = (\omega^2/c^2 - k_{mn}^2)^{1/2} \cong (\omega - l\Omega_c/\gamma)/v_z$, and using Eq. (79), the maximum growth rate for the TE_{mn} mode is shown to be approximately

$$\Gamma_{mnl} = (3^{1/2}/2^{4/3})(\epsilon_{mnnl}^{TE} k_{mn}^4/k_{zmn}\beta_z^2)^{1/3}. \qquad (80)$$

Furthermore, from Eq. (44), the amplitude $\tilde{E}_{mn}(ik_z)$ for the single TE_{mn} mode can be expressed as

$$\frac{\tilde{E}_{mn}(ik_z)}{iE_{mn}(0)} = \frac{k_z(\omega - l\Omega_c/\gamma - k_z v_z)^2 + \epsilon_{mnnl}^{TE} v_z k_{mn}^2 \omega}{(\omega^2/c^2 - k_{mn}^2 - k_z^2)(\omega - l\Omega_c/\gamma - k_z v_z)^2 + \epsilon_{mnnl}^{TE} k_{mn}^2(\omega^2 - c^2 k_z^2)}. \qquad (81)$$

Therefore, the three-dimensional radiation field profile (amplitude and phase) for each individual TE mode can be calculated analytically by the inverse Laplace transform of Eq. (81) with $s = ik_z$. In particular, the rf power in the TE_{mn} mode is given by

$$\frac{P_{mn}(z)}{P_{mn}(0)} = \left|\frac{1}{2\pi i}\int_{\sigma - i\infty}^{\sigma - i\infty} \frac{\tilde{E}_{mn}(s)}{E_{mn}(0)}\exp(sz)ds\right|^2. \qquad (82)$$

Typical gain bandwidth and dependence of rf power on the interaction length z are plotted, respectively, in Figs. 4 and 5.

Figure 4 shows the gain bandwidth for the TE_{11} mode at the fundamental cyclotron frequency ($l = 1$). Here, the solid curve is obtained from Eq. (79). The dots are from the computer simulations using CSPOT. The choice of system parameters corresponds to beam current $I_b = 500$ A, initial pitch angle $\theta_{p0} = p_{\perp 0}/p_{z0} = 0.5$, beam energy $E_b = 1.0$ MeV ($\gamma \cong 2.96$), normalized axial momentum spread $\hat{\sigma}_{pz} = \langle(\hat{p}_z - \langle\hat{p}_z\rangle)^2\rangle^{1/2} = 0$, maximum guiding-center radius $r_m = 0$, waveguide radius $r_w = 1.4$ cm, and axial magnetic field $B_0 = 4.01$ kG. Good agreement is found between linear theory and results from the simulations, except for some discrepancies near the cutoff frequency. Note in Fig. 4

that the spatial growth rate vanishes at $\omega/\omega_{c11} = \omega/ck_{11} \cong 3.8$ due to the cancellation between force bunching and inertial bunching. Indeed, the effective bunching parameter (or effective detuning parameter)[23]
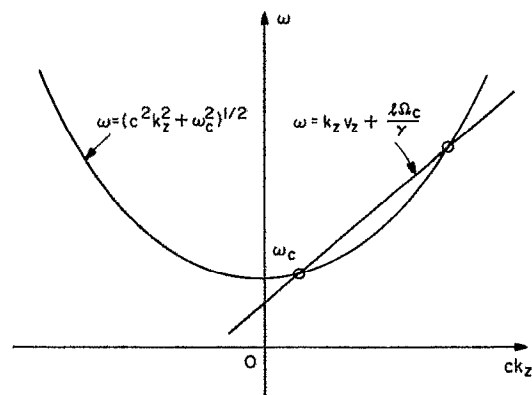

FIG. 3. Schematic of the uncoupled waveguide dispersion relation and the beam cyclotron mode. The CARM interaction occurs near the upshifted intersection of the waveguide and beam modes.
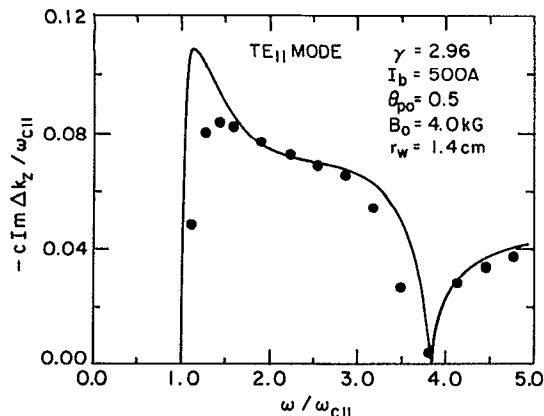
FIG. 4. Gain bandwidth for the TE_{11} mode at the fundamental cyclotron frequency ($l = 1$). The solid curve is obtained from Eq. (79), while the dots are from the simulations using CSPOT. Note that the growth rate vanishes at $\omega/\omega_{c11} \approx 3.8$, where the force bunching cancels the inertial bunching, i.e., $D_{11}^{eff} = 0$ [Eq. (83)].

$$D_{11}^{eff} = 1 - \beta_{\phi11}^2 + \left[\left(\frac{\beta_{\phi11}}{\beta_{z0}} - 1 \right) + \frac{1}{\theta_{p0}^2} \left(\frac{\beta_{\phi11}}{\beta_{z0}} - 1 \right)^2 \right]$$

$$\times \left[1 - \Omega_c/\gamma\omega(1 - \beta_{z0}/\beta_{\phi11}) \right] \qquad (83)$$

vanishes at $\omega/\omega_{c11} \cong 3.8$. Here, D_{11}^{eff} is positive (negative) when $\omega/\omega_{c11} > 3.8 (\omega/\omega_{c11} < 3.8)$.

Figure 5 shows the rf power in the TE_{11} mode as a function of the interaction length z, for the same parameters used in Fig. 4, except that $\omega/\omega_{c11} = 2.87$ ($f = 18$ GHz) is chosen so that the TE_{11} mode is in resonance with the electron beam. In Fig. 5, the solid curve is obtained from the computer simulations, and the dashed curve is calculated analytically from Eqs. (81) and (82). Again, there is good agreement between the linear theory and results from the simulations, even in the launching loss region ($z < 20$ cm).

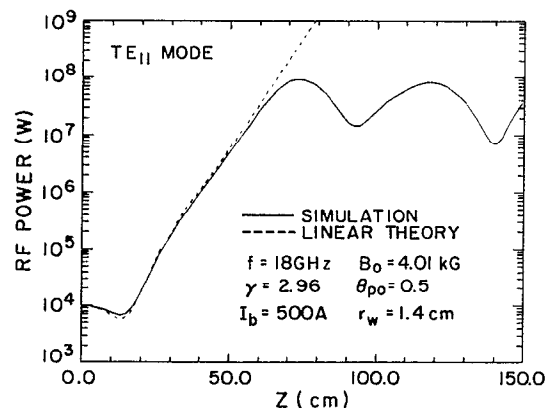We have used our nonlinear, single-mode CARM theory to interpret the recent experimental results from a 35 GHz

FIG. 5. The TE_{11} rf power is plotted as a function of the interaction length z. Here, the system parameters are the same as in Fig. 4, but with $\omega/ck_{11} = 2.87$ ($f = 18$ GHz). The solid curve is from the simulations, while the dashed curve is from Eqs. (81) and (82).
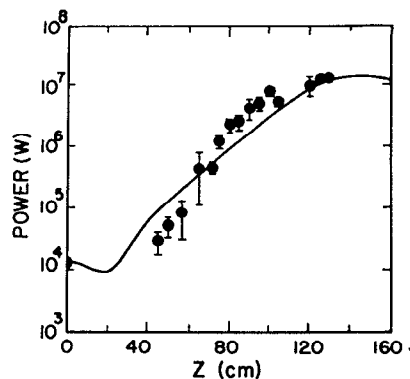

FIG. 6. Comparison of the measured and computed rf power as a function of interaction length for a 35 GHz CARM amplifier experiment operating in the TE_{11} mode.

CARM amplifier.[18,19] In the experiments, an rf power of 12 MW, with an overall gain of 30 dB, has been measured, using a 128 A, 1.5 MeV relativistic electron beam. This amplifier operates in the TE_{11} mode in a cylindrical waveguide. Figure 6 shows the comparison of the measured and computed rf power as a function of interaction length. The system parameters used in the simulation (and in the experiment) correspond to beam energy $E_b = 1.5$ MeV ($\gamma = 3.96$), beam current $I_b = 128$ A, parallel energy spread $\Delta\gamma_{\parallel}/\gamma_{\parallel} = 0.044$ $[\gamma_{\parallel} = (1 - \beta_{z0}^2)^{-1/2}]$, average guiding-center radius $\langle r_g \rangle = 0.15$ cm, initial pitch angle $\theta_{p0} = p_{10}/p_{z0} = 0.27$, axial magnetic field $B_z = 5.4$ kG, waveguide radius $r_w = 0.793$ cm, and an input power of 17 kW. In Fig. 6, the solid curve is from the CSPOT code, while the dotted curve is from the experiment. Good quantitative agreement is found between the theory and the experiment.

B. Single TM mode

Similar analyses can be carried out for a single TM mode. To leading order in $c^2\tilde{k}_{mn}^2/(\omega - l\Omega_c/\gamma - k_z v_z)^2$, it follows from Eqs. (45) and (47) that the dispersion relation for the single TM_{mn} mode is

$$D_{mn}^{TM}(ik_z,\omega) = \omega^2/c^2 - k_z^2 - \tilde{k}_{mn}^2$$

$$+ \epsilon_{mnnl}^{TM} \frac{l(c\tilde{k}_{mn}^2\gamma/l\Omega_c)^2(\beta_z\omega - ck_z)^2}{(\omega - l\Omega_c/\gamma - k_z v_z)^2} = 0, \qquad (84)$$

which is in agreement with earlier results.[12] The maximum growth rate for the TM_{mn} occurs when $\omega^2 - c^2(\tilde{k}_{mn}^2 + k_z^2) \cong 0$ and $\omega - l\Omega_c/\gamma - k_z v_z \cong 0$, and it is given by

$$\tilde{\Gamma}_{mnl} = (3^{1/2}/2^{4/3}l^{1/3})(\epsilon_{mnnl}^{TM}\tilde{k}_{mn}^2\tilde{k}_{zmn})^{1/3}$$

$$\times (c\tilde{k}_{mn}\gamma/\Omega_c)^{2/3}(1 - 1/\beta_z\tilde{\beta}_{\phi mn})^{2/3}. \qquad (85)$$

Note in Eq. (85) that $\tilde{\Gamma}_{mnl}$ vanishes when $\beta_z\tilde{\beta}_{\phi mn} = 1$, as pointed out by several authors.[12,30,31] From Eq. (45), the amplitude $\tilde{B}_{mn}(ik_z)$ for the TM_{mn} mode can be expressed as

$$\frac{\widetilde{B}_{mn}(ik_z)}{iB_{mn}(0)} = \frac{k_z(\omega - l\Omega_c/\gamma - k_z v_z)^2 + \epsilon_{mnnl}^{TM}(c\bar{k}_{mn}^2 \gamma\omega/l\Omega_c)(\beta_z\omega - ck_z)}{(\omega^2/c^2 - \bar{k}_{mn}^2 - k_z^2)(\omega - l\Omega_c/\gamma - k_z v_z)^2 + \epsilon_{mnnl}^{TM}l(c\bar{k}_{mn}^2\gamma/l\Omega_c)^2(\beta_z\omega - ck_z)^2}, \tag{86}$$

which can be used to calculate the radiation field profile and power. Typical gain bandwidth and dependence of rf power on the interaction length, z, are plotted, respectively, in Figs. 7 and 8.

Figure 7 shows the gain bandwidth for the TM_{11} mode at the fundamental cyclotron frequency ($l = 1$) with system parameters: $I_b = 500$ A, $\theta_{p0} = 0.6$, $\gamma = 2.96$, $\hat{\sigma}_{pz} = 0$, $r_m = 0$, $r_w = 1.4$ cm, and $B_0 = 8.45$ kG. Here, the solid curve is obtained from Eq. (84), and the dotted curve is from the computer simulations. Note in Fig. 7 that the gain bandwidth consists of two frequency domains separated by the condition $\beta_{z0}\tilde{\beta}_{\phi11} = 1$ at $\omega/\tilde{\omega}_{c11} = \omega/c\bar{k}_{11} \cong 1.7$. Figure 8 depicts the rf power in the TM_{11} as a function of z, for the same parameters used in Fig. 7, except that $\omega/\tilde{\omega}_{c11} = 1.38$ ($f = 18$ GHz) is chosen so that the TM_{11} mode is in resonance with the electron beam. In Fig. 8, the solid curve is obtained from the computer simulations, and the dashed curve is calculated using Eq. (86).

VI. NUMERICAL ANALYSIS FOR MULTIPLE MODES

In this section, we use linear and nonlinear theory in Secs. III and IV to analyze the multimode CARM interac-

tion with two or more waveguide modes, and to illustrate the general features of multimode phenomena in an overmoded CARM amplifier. We show analytically that all of the coupled waveguide modes grow with the dominant unstable mode at the same growth rate, and that the phases of coupled modes are locked in the exponential gain regime, and remain approximately locked for some finite interaction length beyond saturation. The simulations indicate that the saturated power in each mode is insensitive to input rf power distribution among the coupled modes, but is sensitive to detuning.

A. Two-mode coupling

We first examine the CARM interaction with the TE_{mn} and $TE_{mn'}$ waveguide modes coupling to a cold, thin ($k_{mn}r_g \ll 1$ and $k_{mn'}r_g \ll 1$), azimuthally symmetric electron beam at a given harmonic cyclotron frequency $l\Omega_c/\gamma$. In this case, the general matrix equation in Eqs. (44) and (45) reduces to a 2×2 matrix equation of the form

$$M\begin{pmatrix}\widetilde{E}_{mn}(s) \\ \widetilde{E}_{mn'}(s)\end{pmatrix} = S\begin{pmatrix}E_{mn}(0) \\ E_{mn'}(0)\end{pmatrix}, \tag{87}$$

where the 2×2 matrices M and S are defined by

$$M = \begin{pmatrix} D_{mn}^{TE}(s,\omega) & \epsilon_{mnn'l}^{TE}k_{mn'}^2(\omega^2 + c^2s^2)\Delta^{-2} \\ \epsilon_{mn'nl}^{TE}k_{mn}^2(\omega^2 + c^2s^2)\Delta^{-2} & D_{mn'}^{TE}(s,\omega) \end{pmatrix}, \tag{88}$$

$$S = \begin{pmatrix} s + i\epsilon_{mnnl}^{TE}v_z k_{mn}^2\omega\Delta^{-2} & i\epsilon_{mnn'l}^{TE}v_z k_{mn'}^2\omega\Delta^{-2} \\ i\epsilon_{mn'nl}^{TE}v_z k_{mn}^2\omega\Delta^{-2} & s + i\epsilon_{mn'n'l}^{TE}v_z k_{mn'}^2\omega\Delta^{-2} \end{pmatrix}, \tag{89}$$
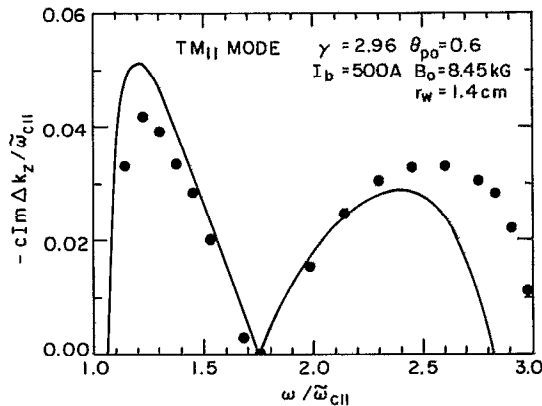

FIG. 7. Gain bandwidth for the TM_{11} mode at the fundamental cyclotron frequency ($l = 1$). The solid curve is obtained from Eq. (84), while the dotted curve is from the simulations. Note that the gain bandwidth consists of two frequency domains separated when the condition $\beta_{z0}\beta_{\phi11} = 1$ is satisfied at $\omega/\omega_{c11} \cong 1.7$, and that the simplified dispersion relation in Eq. (84) is not valid far off resonance ($\omega/\tilde{\omega}_{c11} > 2.0$).
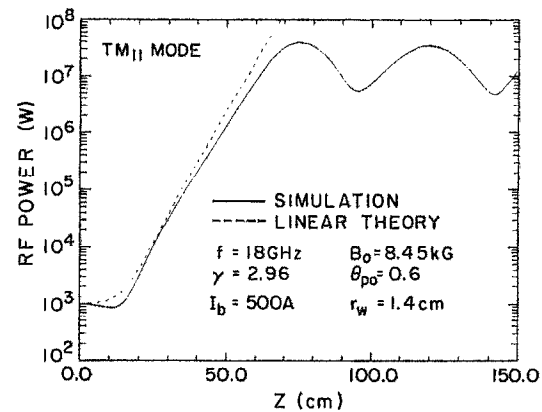

FIG. 8. The TM_{11} rf power is plotted as a function of the interaction length z. The system parameters are the same as in Fig. 7 with $\omega/c\bar{k}_{11} = 1.38$ ($f = 18$ GHz). The solid curve is from the simulations, while the dashed curve is from Eq. (86).

and $\Delta = \Delta(s,\omega) = \omega - l\Omega_c/\gamma + isv_z$. Here, $D_{mn}^{TE}(s,\omega)$ is defined in Eq. (46), and $\epsilon_{mnn'l}^{TE}$ in Eq. (48). Solving Eq. (87) for $\widetilde{E}_{mn}(s)$ and $\widetilde{E}_{mn'}(s)$ yields

$$\begin{pmatrix} \widetilde{E}_{mn}(s) \\ \widetilde{E}_{mn'}(s) \end{pmatrix} = M^{-1}S\begin{pmatrix} E_{mn}(0) \\ E_{mn'}(0) \end{pmatrix}, \qquad (90)$$

where

$$M^{-1} = \frac{1}{\det M}\begin{pmatrix} m_{22} & -m_{12} \\ -m_{21} & m_{11} \end{pmatrix} \qquad (91)$$

is the inverse of M, and m_{ij} are the elements of M. Therefore, the three-dimensional radiation field profile and power are readily calculated by the inverse Laplace transform of $\widetilde{E}_{mn}(s)$ in Eq. (90). Note that the singularities in the integrand of the inverse Laplace transform of $\widetilde{E}_{mn}(s)$ are determined from the dispersion relation

$$\det M = 0, \qquad (92)$$

for the coupled TE_{mn} and $TE_{mn'}$ modes. Making use of the relation $\epsilon_{mnn'l}^{TE}\epsilon_{mn'nl}^{TE} = \epsilon_{mnnl}^{TE}\epsilon_{mn'n'l}^{TE}$, and substituting $s = ik_z$, the coupled-mode dispersion relation in Eq. (92) can be expressed as[10]

$$\left(k_z^2 + k_{mn}^2 - \frac{\omega^2}{c^2}\right)\left(k_z^2 + k_{mn'}^2 - \frac{\omega^2}{c^2}\right)$$
$$\times\left(\omega - \frac{l\Omega_c}{\gamma} - k_z v_z\right)^2$$
$$= \left[\epsilon_{mnnl}^{TE}k_{nn}^2(k_z^2 + k_{mn'}^2 - \omega^2/c^2)\right.$$
$$\left. + \epsilon_{mn'n'l}^{TE}k_{n'n'}^2(k_z^2 + k_{mn}^2 - \omega^2/c^2)\right](\omega^2 - c^2k_z^2), \qquad (93)$$

which is a sixth-order polynomial of k_z with real coefficients and therefore has six roots. When the two waveguide modes are well separated, and

$$\epsilon_{mnnl}^{TE}k_{nn}^2(k_z^2 + k_{mn'}^2 - \omega^2/c^2)$$
$$\gg \epsilon_{mn'n'l}^{TE}k_{n'n'}^2(k_z^2 + k_{mn}^2 - \omega^2/c^2), \qquad (94)$$

corresponding to the beam cyclotron mode, $\omega = k_z v_z + l\Omega_c/\gamma$, resonant with the TE_{mn} waveguide mode, $\omega = c(k_z^2 + k_{mn}^2)^{1/2}$, Eq. (93) becomes the usual single-mode dispersion relation, Eq. (79).

Typical results from the computer simulations and (linear) kinetic theory are summarized in Figs. 9–12. Figure 9 shows the dependence of rf power in the TE_{11} and TE_{12} modes on the interaction length z, for (a) single-mode CARM interactions and (b) the CARM interaction with both modes coupling to the beam. The system parameters in Fig. 9 are frequency $f = 18$ GHz, beam current $I_b = 500$ A, beam energy $E_b = 1.0$ MeV ($\gamma = 2.96$), initial pitch angle $\theta_{p0} = \beta_{\perp 0}/\beta_{z0} = 0.6$, normalized axial momentum spread $\hat{\sigma}_{pz} = 0$, maximum guiding-center radius $r_m = 0$, waveguide radius $r_w = 2.7$ cm, and axial magnetic field $B_0 = 3.92$ kG, corresponding to the TE_{11} mode in resonance, and the TE_{12} mode off resonance, with the electron beam at the fundamental cyclotron frequency ($l = 1$).

In Fig. 9, the solid curves are the results obtained from the computer simulations using CSPOT with 1024 particles. The dashed curves in Fig. 9(a) are obtained analytically
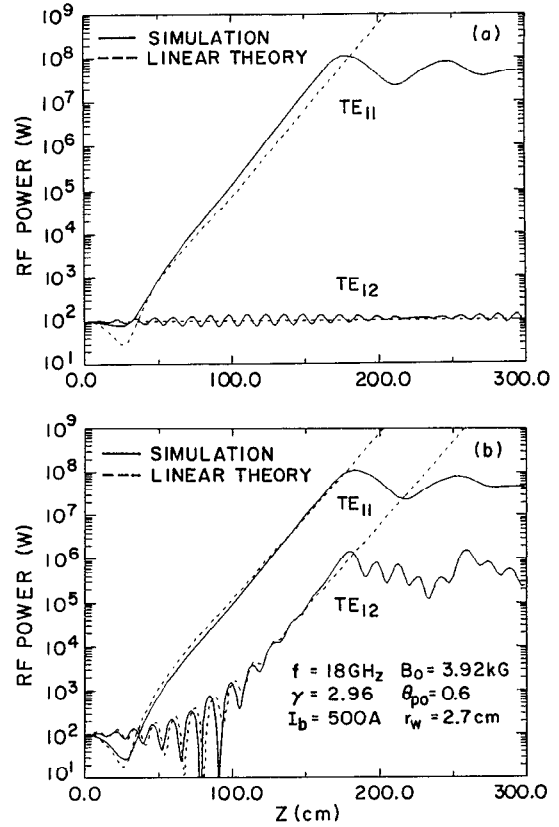

FIG. 9. The rf power in the TE_{11} and TE_{12} is plotted as a function of interaction length for (a) single-mode CARM interactions and (b) the CARM interaction with the two waveguide modes coupling to the electron beam. Note that in Fig. 8(b), the TE_{12} mode grows with the dominant unstable TE_{11} mode at the same growth rate due to mode coupling, despite the differences in launching losses.

from the single-mode linear theory [Eq. (81)], while the dashed curves in Fig. 9(b) are from the multimode linear theory [Eq. (90)]. The inclusion of the coupling of the TE_{11} and TE_{12} modes results in the instability of the TE_{12} mode, as seen in Fig. 9(b), while the single-mode theory would predict stability for the TE_{12} mode, as seen in Fig. 9(a). In
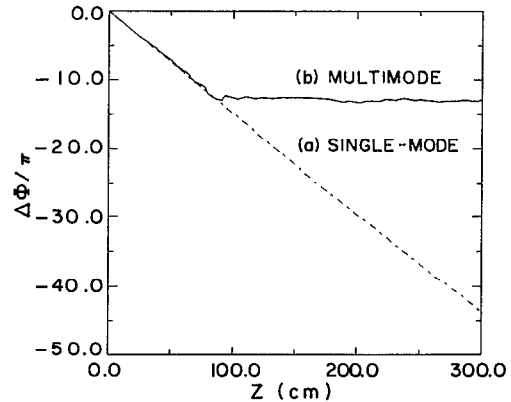

FIG. 10. The relative rf phase $\Delta\Phi = (k_{z12} - k_{z11})z + \delta_{12}(z) - \delta_{11}(z)$ is plotted as a function of the interaction length z. Here, the two curves, (a) and (b), correspond to the single-mode simulations in Fig. 9(a), and to the multimode simulation in Fig. 9(b), respectively.
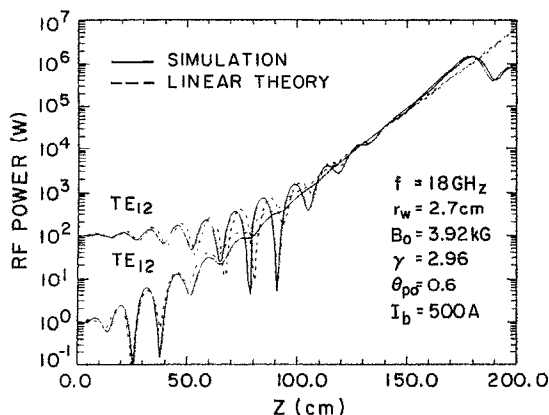
C. Chen and J. S. Wurtele   2143

FIG. 11. The TE_{12} rf power is plotted as a function of the interaction length z for a CARM with the TE_{11} and TE_{12} modes. The two solid curves depict the linear and nonlinear evolution of rf power in the TE_{12} mode obtained from the simulations with two input rf power distributions: (a) $P_0(TE_{11}) = P_0(TE_{12}) = 100$ W, and (b) $P_0(TE_{11}) = 100$ W and $P_0(TE_{12}) = 1$ W, while the dashed curves are the corresponding analytical results from Eq. (90).
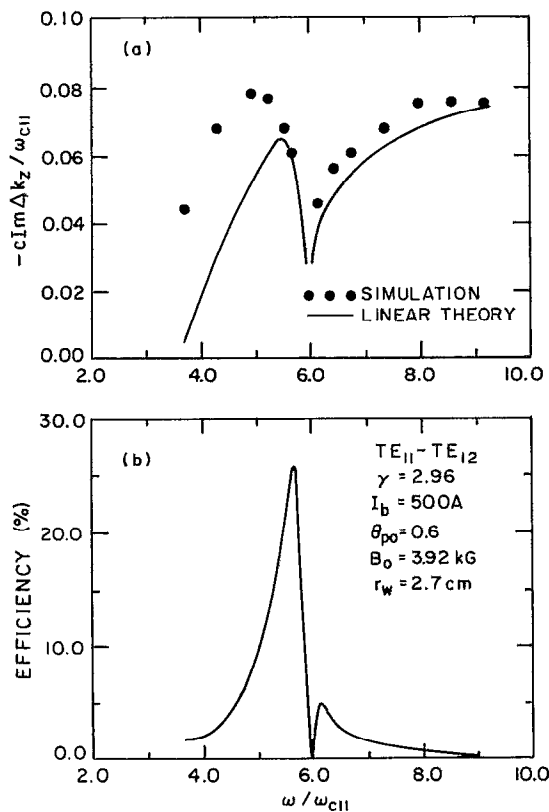

FIG. 12. (a) Gain bandwidth for the CARM interaction with the TE_{11} and TE_{12} modes coupling to the electron beam for the same system parameters used in Figs. 9(b) and 10(b), except that ω varies from $3\omega_{c11}$ to $9\omega_{c11}$. Here, the solid curve is obtained from the approximate dispersion relation (93), while the dots are results from the simulations. (b) The saturated efficiency is plotted as a function of frequency for the same system, as obtained from the simulations.

fact, in Fig. 9(b), the TE_{12} mode grows with the dominant unstable TE_{11} mode, and the two coupled modes have the same spatial growth rate, $-\,\text{Im}\,\Delta k_z > 0$, corresponding to the most unstable solution of the coupled-mode dispersion relation in Eq. (93). Because the TE_{11} mode is in resonance with the electron beam and the TE_{12} mode is detuned from resonance, the TE_{12} mode suffers greater launching losses than the TE_{11} mode. Excellent agreement is found between the simulation and linear theory in the linear regime. In particular, numerous amplitude oscillations of the TE_{12} mode are well described by our linear theory throughout the launching loss region, from $z = 0$ to $z \cong 100$ cm, as is evident in Fig. 9(b).

The evolution of relative rf phase, $\Delta\Phi(z) = \Phi_{12} - \Phi_{11} = (k_{z12} - k_{z11})z + \delta_{12}(z) - \delta_{11}(z)$, is plotted as a function of z in Fig. 10, for the simulations used in Fig. 9. In Fig. 10, the dashed curve, designated by label (a), is obtained by subtracting the rf phases which result from the single-mode simulations of the TE_{11} mode and of the TE_{12} mode used in Fig. 9(a); the solid curve, designated by label (b), is calculated by subtracting the rf phases in the multimode simulation of Fig. 9(b). As a result of the mode coupling, the relative rf phase $\Delta\Phi(z)$, as shown in Fig. 10(b), is approximately constant (with variation less than 0.2π) in the exponential gain regime from $z \cong 100$ cm to $z \cong 175$ cm, which we refer to as *phase locking*. The phenomenon of phase locking of transverse modes in the exponential gain regime is predicted by linear theory, because the multimode dispersion relation in Eq. (93) yields a unique k_z, with a negative imaginary part, which determines the growth rate and phase shifts for all the coupled modes. What is more remarkable is that phase locking (with phase variation less than 0.6π) persists even in the nonlinear region, (at least for some finite interaction length beyond saturation), as seen in Fig. 10(b).

Figures 9(b) and 10(b) reveal two general features of the multimode CARM interaction: (1) all of the coupled waveguide modes have the same small-signal growth rate, and suffer different launching losses, which depend strongly upon the detuning; (2) the phases of coupled modes are locked in the exponential gain regime, and remain approximately locked for some interaction length beyond saturation.

Another interesting feature of the multimode CARM interaction is that the saturated rf power of each mode is *insensitive* to input rf power distribution among the coupled modes at $z = 0$. Figure 11 shows the results of simulations for the coupled TE_{11} and TE_{12} modes with two different distributions of input rf power. In Fig. 11, the two solid curves depict the linear and nonlinear evolution of the rf power in the TE_{12} mode that was generated by the simulations with input power distributions: (a) $P_0(TE_{11}) = P_0(TE_{12}) = 100$ W, and (b) $P_0(TE_{11}) = 100$ W and $P_0(TE_{12}) = 1$ W; the two dashed curves are the corresponding analytical results from Eq. (90). Here, only the TE_{12} mode is plotted, because the TE_{11} mode remains virtually unchanged for the two distributions.

The gain bandwidth and efficiency are plotted in Fig. 12, for the coupled TE_{11} and TE_{12} modes, with the same system

parameters used in Figs. 9(b) and 10(b), except that ω varies from $3\omega_{c11}$ to $9\omega_{c11}$. The efficiency is defined by $\eta = (\gamma_0 - \langle\gamma\rangle)/(\gamma_0 - 1)$. In Fig. 12(a), the solid curve shows the growth rate from the simulations; the dashed curve is the corresponding analytical result predicted from Eq. (93). Quantitative agreement is found for $\omega/\omega_{c11} > 5.5$, while only qualitative agreement can be found for $\omega/\omega_{c11} < 5.5$. As is the case of the single-mode CARM interaction discussed in Sec. V A, the gain bandwidth for the two coupled modes consists of two frequency domains. Although the growth rates in both domains are comparable, as seen in Fig. 12(a), it is shown in Fig. 12(b) that efficiency reaches a sharp maximum of approximately 26% at $\omega/\omega_{c11} \cong 5.8$ ($f \cong 18.5$ GHz), corresponding to the TE_{11} mode being nearly resonant with the electron beam. Note in Fig. 12(b) that there is a small peak at $\omega/\omega_{c11} \cong 6.0$ in the high frequency domain, which is also true in the corresponding single-mode CARM interaction.

Another example is shown in Figs. 13 and 14, where we plot the dependence of rf power and relative rf phase on the interaction length z for a CARM with the TE_{11} and TM_{11} modes. In Figs. 13 and 14, the system parameters are $f = 18$ GHz, $I_b = 500$ A, $\gamma = 2.96$, $\theta_{p0} = \beta_{10}/\beta_{z0} = 0.6$, $\hat{\sigma}_{pz} = 0$, $r_m = 0$, $r_w = 1.7$ cm, and $B_0 = 4.84$ kG, corresponding to the TE_{11} mode in resonance, and the TM_{11} mode off resonance, with the electron beam at the fundamental cyclotron frequency. The general features of the coupling of the TE_{11} and TE_{12} modes [Figs. 9(b) and 10(b)] hold true also for the coupling of the TE_{11} and TM_{11} modes, as shown in Figs. 13 and 14.

B. Many-mode coupling

The multimode CARM interaction with more than two waveguide modes can be analyzed with the same method as two-mode coupling. Here, we only present the detuning characteristics of a CARM amplifier with four coupled TE_{1n} modes ($n = 1,2,3,4$). Figure 15 depicts the dependence of
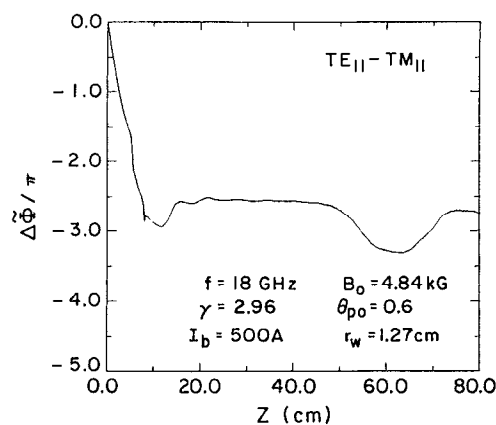

FIG. 14. The relative rf phase $\Delta\tilde{\Phi} = (\tilde{k}_{z11} - k_{z11})z + \tilde{\delta}_{11}(z) - \delta_{11}(z)$ is plotted as a function of the interaction length z, as obtained from the simulation for the same parameters as in Fig. 13.

the (fractional) saturated TE_{1n} power on the axial magnetic field B_0, as obtained from the simulation with an input power of 100 W per mode. By increasing the axial magnetic field B_0 in Fig. 15, the beam mode is successively tuned through the resonances with the TE_{11}, TE_{12}, TE_{13}, and TE_{14} modes at $B_0 = 3.74, 4.29, 5.33$, and 6.98 kG, respectively. The fractional rf power for a given mode at saturation reaches a maximum at its resonant magnetic field, and then decreases rapidly off resonance. In the transition from one resonance to another, however, two adjacent competing modes can have comparable rf power levels at saturation.

Figure 16 shows the dependence of the TE_{1n} rf power on the interaction length, for the choice of system parameters used in Fig. 16. Here, the value of magnetic field $B_0 = 5.33$ kG corresponds to the TE_{13} mode in resonance with the electron beam. Again, the growth rates are the same for all of the coupled modes, as in the two-mode coupling shown in Figs. 9(b) and 13.
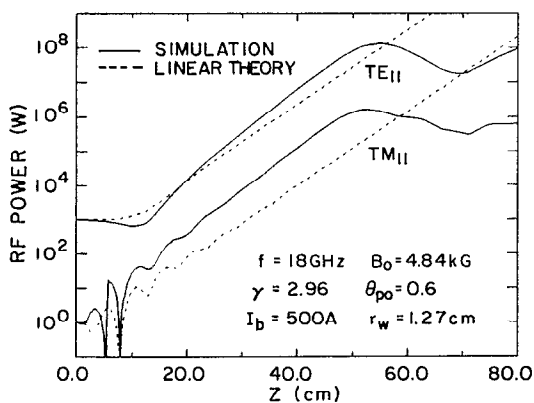

FIG. 13. The rf power is plotted as a function of the interaction length z for a CARM with the TE_{11} and TM_{11} modes. Here, the choice of system parameters corresponds to the TE_{11} mode in resonance, and the TM_{11} mode off resonance, with the electron beam. The solid curve is obtained from the simulation, while the dashed curve is from the multimode linear theory.
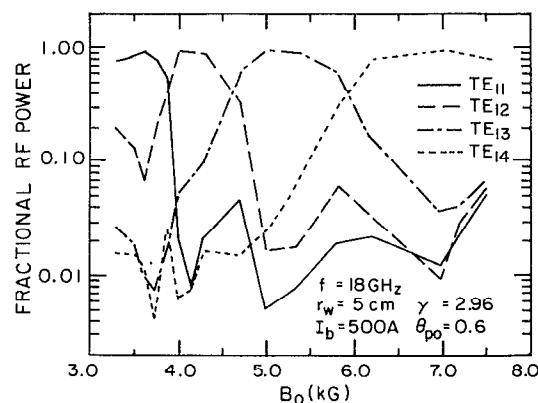

FIG. 15. The fractional rf power at saturation in four coupled TE_{1n} modes is plotted as a function of the axial magnetic field B_0. Here, the values of the resonant magnetic field for the TE_{11}, TE_{12}, TE_{13}, and TE_{14} modes correspond to $B_0 = 3.74, 4.29, 5.33$, and 6.98 kG, respectively.
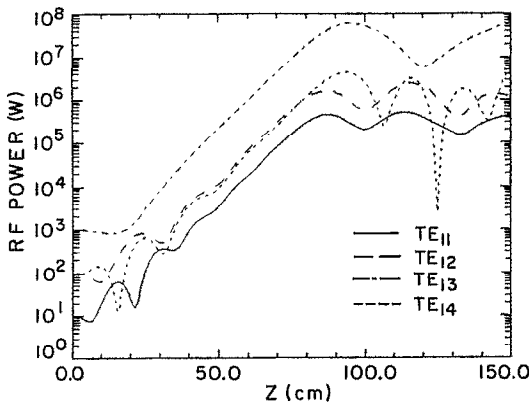
C. Chen and J. S. Wurtele   2145

FIG. 16. The rf power in four coupled TE_{1n} modes is plotted as a function of the interaction length z, as obtained from the simulation for the system used in Fig. 15. Here, the value of the magnetic field $B_0 = 5.33$ kG corresponds to the TE_{13} mode in resonance with the electron beam.

VII. CONCLUSIONS

In conclusion, we have presented a general treatment of multiple waveguide mode interactions in an overmoded cyclotron autoresonance maser amplifier using kinetic theory and a fully nonlinear, three-dimensional, self-consistent model. Good agreement has been found between the simulations and theory in the linear regime. The general features of multimode phenomena have been illustrated in the linear and nonlinear regimes.

It was shown analytically, and confirmed in the simulations, that all of the coupled waveguide modes grow with the dominant unstable mode at the same spatial growth rate, but suffer different launching losses which depend upon detuning. The phases of coupled modes are locked in the exponential gain regime, and remain approximately locked for some finite interaction length beyond saturation.

The saturated rf power in each mode was found to be insensitive to input rf power distribution among the coupled modes, but it is sensitive to detuning. Simulations indicated that the fractional rf power for a given mode at saturation reaches a maximum at its resonant magnetic field, then decreases rapidly off resonance.

As a general conclusion, based on the results of this paper, an accurate calculation of the growth rate, saturation levels, and radiation field profile in overmoded CARM amplifiers requires the use of a multimode theory in the linear and nonlinear regimes. We believe that the present analysis can be generalized to treat multimode phenomena in a large class of free-electron amplifiers including free-electron lasers, gyrotron traveling-wave tubes, and Čerenkov masers. It can be easily extended to include nonaxisymmetric beams and, with more effort, used to study high-gain overmoded oscillators.

APPENDIX A: MODE DECOMPOSITION FOR THE LINEARIZED VLASOV EQUATION

To derive Eq. (28) from Eq. (27), we follow Refs. 12 and 22 and make use of recurrence relations and Graf's theorem for Bessel functions[27] to express the radiation field components in Eq. (27). It is straightforward to show from Eqs. (8)–(11) that

$$
\begin{aligned}
E_\perp &= E_r \cos(\phi - \theta) + E_\theta \sin(\phi - \theta) \\
&= \frac{1}{2} \sum_{mnq} \exp[i\Lambda_{mq}(\phi,\phi_c,t)] \left[k_{mn} C_{mn} X_{mnq} E_{mn}(z) \right. \\
&\quad \left. + \check{k}_{mn} \widetilde{C}_{mn} \widetilde{X}_{mnq} \left(\frac{ic}{\omega}\right) \frac{dB_{mn}(z)}{dz} \right] + \text{c.c.},
\end{aligned}
\tag{A1}
$$

$$
\begin{aligned}
E_\perp \cos\phi_c &- E_\phi \sin\phi_c \\
&= E_r \cos(\phi - \theta - \phi_c) + E_\theta \sin(\phi - \theta - \phi_c) \\
&= \frac{1}{2} \sum_{mnq} \exp[i\Lambda_{mq}(\phi,\phi_c,t)] \\
&\quad \times \left[- k_{mn} C_{mn} Y_{mnq} E_{mn}(z) \right. \\
&\quad \left. + \check{k}_{mn} \widetilde{C}_{mn} \widetilde{Y}_{mnq} \left(\frac{ic}{\omega}\right) \frac{dB_{mn}(z)}{dz} \right] + \text{c.c.},
\end{aligned}
\tag{A2}
$$

$$
\begin{aligned}
E_z &= \frac{1}{2} \sum_{mnq} \exp[i\Lambda_{mq}(\phi,\phi_c,t)] \check{k}_{mn} \widetilde{C}_{mn} \widetilde{X}_{mnq} \\
&\quad \times [c\check{k}_{mn}^2 r_L/(m+q)\omega] B_{mn}(z) + \text{c.c.},
\end{aligned}
\tag{A3}
$$

$$
\begin{aligned}
B_\phi &= - B_r \sin(\phi - \theta) + B_\theta \cos(\phi - \theta) \\
&= \frac{1}{2} \sum_{mnq} \exp[i\Lambda_{mq}(\phi,\phi_c,t)] \left[- k_{mn} C_{mn} X_{mnq} \right. \\
&\quad \left. \times \left(\frac{ic}{\omega}\right) \frac{dE_{mn}(z)}{dz} - \check{k}_{mn} \widetilde{C}_{mn} \widetilde{X}_{mnq} B_{mn}(z) \right] + \text{c.c.},
\end{aligned}
\tag{A4}
$$

$$
\begin{aligned}
B_\perp &\sin\phi_c + B_\phi \cos\phi_c \\
&= - B_r \sin(\phi - \theta - \phi_c) + B_\theta \cos(\phi - \theta - \phi_c) \\
&= \frac{1}{2} \sum_{mnq} \exp[i\Lambda_{mq}(\phi,\phi_c,t)] \\
&\quad \times \left[k_{mn} C_{mn} Y_{mnq} \left(\frac{ic}{\omega}\right) \frac{dE_{mn}(z)}{dz} \right. \\
&\quad \left. - \check{k}_{mn} \widetilde{C}_{mn} \widetilde{Y}_{mnq} B_{mn}(z) \right] + \text{c.c.},
\end{aligned}
\tag{A5}
$$

$$
\begin{aligned}
B_z \sin\phi_c &= \frac{1}{2} \sum_{mnq} \exp[i\Lambda_{mq}(\phi,\phi_c,t)] k_{mn} C_{mn} Z_{mnq} \\
&\quad \times (ck_{mn}/2\omega) E_{mn}(z) + \text{c.c.},
\end{aligned}
\tag{A6}
$$

where $\Lambda_{mq}(\phi,\phi_c,t) = m\phi + q\phi_c - \omega t - m\pi/2$, and the geometric factors X, Y, Z, $\tilde{X}$, and $\tilde{Y}$ are defined in Eqs. (31)–(35). Substituting Eqs. (A1)–(A6) into Eq. (27) and performing some algebra then yields Eq. (28).

APPENDIX B: DERIVATION OF LINEARIZED AMPLITUDE EQUATIONS

The linearized amplitude equations (44) and (45) can be derived as follows. Multiplying Eqs. (40) and (41) with $\exp(-sz)$ and integrating over z, respectively, some straightforward algebra then yields

$$D_{mn}^{\mathrm{TE}}(s,\omega)\tilde{E}_{mn}(s) - \sum_{n'(n'\neq n)}\sum_{l=-\infty}^{\infty}\left[\chi_{mnn'l}^{\mathrm{TE}}\tilde{E}_{mn'}(s)\right.$$
$$\left. + \chi_{mnn'l}^{\mathrm{EM}}\tilde{B}_{mn'}(s)\right]$$
$$= sE_{mn}(0) + \sum_{n'}\sum_{l=-\infty}^{\infty}\left[\mu_{mnn'l}^{\mathrm{TE}}E_{mn'}(0)\right.$$
$$\left. + \mu_{mnn'l}^{\mathrm{EM}}B_{mn'}(0)\right], \tag{B1}$$

$$D_{mn}^{\mathrm{TM}}(s,\omega)\tilde{B}_{mn}(s) - \sum_{n'(n'\neq n)}\sum_{l=-\infty}^{\infty}\left[\chi_{mnn'l}^{\mathrm{ME}}\tilde{E}_{mn'}(s)\right.$$
$$\left. + \chi_{mnn'l}^{\mathrm{TM}}\tilde{B}_{mn'}(s)\right]$$
$$= sB_{mn}(0) + \sum_{n'}\sum_{l=-\infty}^{\infty}\left[\mu_{mnn'l}^{\mathrm{ME}}E_{mn'}(0)\right.$$
$$\left. + \mu_{mnn'l}^{\mathrm{TM}}B_{mn'}(0)\right]. \tag{B2}$$

In Eqs. (B1) and (B2),

$$D_{mn}^{\mathrm{TE}}(s,\omega) = s^2 - k_{mn}^2 + \frac{\omega^2}{c^2} - \sum_{l=-\infty}^{\infty}\chi_{mnnl}^{\mathrm{TE}}(s,\omega) \tag{B3}$$

and

$$D_{mn}^{\mathrm{TM}}(\omega) = s^2 - \tilde{k}_{mn}^2 + \frac{\omega^2}{c^2} - \sum_{l=-\infty}^{\infty}\chi_{mnnl}^{\mathrm{TM}}(s,\omega) \tag{B4}$$

are the TE_{mn} and TM_{mn} dielectric functions, respectively; the susceptibility functions are defined by

$$\chi_{mnn'l}^{\mathrm{TE}}(s,\omega) = -\frac{16\pi^3 e^2 \omega k_{mn'}^2}{c}\left(\frac{C_{mn}}{k_{mn}}\right)\left(\frac{C_{mn'}}{k_{mn'}}\right)\int r_g\, dr_g\, X_{mnl-m}\int p_\perp\, dp_\perp\, dp_z\, \frac{\beta_\perp}{\omega - l\Omega_c/\gamma + isv_z}$$
$$\times\left\{X_{mn'l-m}\left[\left(1+\frac{isv_z}{\omega}\right)\frac{\partial f_0}{\partial p_\perp} - \frac{isv_\perp}{\omega}\frac{\partial f_0}{\partial p_z}\right] - \left[\frac{Y_{mn'l-m}}{m_0\Omega_c}\left(1+\frac{isv_z}{\omega}\right) - \frac{Z_{mn'l-m}}{m_0\Omega_c}\left(\frac{k_{mn'}v_\perp}{2\omega}\right)\right]\frac{\partial f_0}{\partial r_g}\right\}, \tag{B5}$$

$$\chi_{mnn'l}^{\mathrm{EM}}(s,\omega) = -\frac{16\pi^3 e^2 \omega \tilde{k}_{mn'}^2}{c}\left(\frac{C_{mn}}{k_{mn}}\right)\left(\frac{\tilde{C}_{mn'}}{\tilde{k}_{mn'}}\right)\int r_g\, dr_g\, X_{mnl-m}\int p_\perp\, dp_\perp\, dp_z\, \frac{\beta_\perp}{\omega - l\Omega_c/\gamma + isv_z}$$
$$\times\left\{\tilde{X}_{mn'l-m}\left[\left(\beta_z+\frac{ics}{\omega}\right)\frac{\partial f_0}{\partial p_\perp} - \left(\beta_\perp - \frac{c\tilde{k}_{mn'}^2 r_L}{l\omega}\right)\frac{\partial f_0}{\partial p_z}\right] + \frac{\tilde{Y}_{mn'l-m}}{m_0\Omega_c}\left(\beta_z+\frac{ics}{\omega}\right)\frac{\partial f_0}{\partial r_g}\right\}, \tag{B6}$$

$$\chi_{mnn'l}^{\mathrm{TM}}(s,\omega) = -\frac{16\pi^3 e^2 \omega^2 \tilde{k}_{mn'}^2}{c^2 \tilde{k}_{mn}}\left(\frac{\tilde{C}_{mn}}{\tilde{k}_{mn}}\right)\left(\frac{\tilde{C}_{mn'}}{\tilde{k}_{mn'}}\right)\int r_g\, dr_g\, \frac{\tilde{k}_{mn}r_L}{l}\tilde{X}_{mnl-m}\int p_\perp\, dp_\perp\, dp_z\, \frac{(\beta_z+ics/\omega)}{\omega - l\Omega_c/\gamma + isv_z}$$
$$\times\left\{\tilde{X}_{mn'l-m}\left[\left(\beta_z+\frac{ics}{\omega}\right)\frac{\partial f_0}{\partial p_\perp} - \left(\beta_\perp - \frac{c\tilde{k}_{mn'}^2 r_L}{l\omega}\right)\frac{\partial f_0}{\partial p_\perp}\right] + \frac{\tilde{Y}_{mn'l-m}}{m_0\Omega_c}\left(\beta_z+\frac{ics}{\omega}\right)\frac{\partial f_0}{\partial r_g}\right\}, \tag{B7}$$

$$\chi_{mnn'l}^{\mathrm{ME}}(s,\omega) = -\frac{16\pi^3 e^2 \omega^2 k_{mn'}^2}{c^2 \tilde{k}_{mn}}\left(\frac{\tilde{C}_{mn}}{\tilde{k}_{mn}}\right)\left(\frac{C_{mn'}}{k_{mn'}}\right)\int r_g\, dr_g\, \frac{\tilde{k}_{mn}r_L}{l}\tilde{X}_{mnl-m}\int p_\perp\, dp_\perp\, dp_z\, \frac{(\beta_z+ics/\omega)}{\omega - l\Omega_c/\gamma + isv_z}$$
$$\times\left\{X_{mn'l-m}\left[\left(1+\frac{isv_z}{\omega}\right)\frac{\partial f_0}{\partial p_\perp} - \frac{isv_\perp}{\omega}\frac{\partial f_0}{\partial p_z}\right] - \left[\frac{Y_{mn'l-m}}{m_0\Omega_c}\left(1+\frac{isv_z}{\omega}\right) - \frac{Z_{mn'l-m}}{m_0\Omega_c}\left(\frac{k_{mn'}v_\perp}{2\omega}\right)\right]\frac{\partial f_0}{\partial r_g}\right\}. \tag{B8}$$

Moreover, the μ's are defined by

$$\mu_{mnn'l}^{\mathrm{TE}}(s,\omega) = i16\pi^3 e^2 k_{mn'}^2\left(\frac{C_{mn}}{k_{mn}}\right)\left(\frac{C_{mn'}}{k_{mn'}}\right)$$
$$\times\int r_g\, dr_g\, X_{mnl-m}\int p_\perp\, dp_\perp\, dp_z$$
$$\times\frac{\beta_\perp\beta_z}{\omega - l\Omega_c/\gamma + isv_z}$$
$$\times\left(X_{mn'l-m}\frac{\partial f_0}{\partial p_\perp} - \frac{Y_{mn'l-m}}{m_0\Omega_c}\frac{\partial f_0}{\partial r_g}\right), \tag{B9}$$

$$\mu_{mnn'l}^{\mathrm{EM}}(s,\omega) = i16\pi^3 e^2 \tilde{k}_{mn'}^2\left(\frac{C_{mn}}{k_{mn}}\right)\left(\frac{\tilde{C}_{mn'}}{\tilde{k}_{mn'}}\right)$$
$$\times\int r_g\, dr_g\, X_{mnl-m}\int p_\perp\, dp_\perp\, dp_z$$
$$\times\frac{\beta_\perp}{\omega - l\Omega_c/\gamma + isv_z}$$
$$\times\left(\tilde{X}_{mn'l-m}\frac{\partial f_0}{\partial p_\perp} + \frac{\tilde{Y}_{mn'l-m}}{m_0\Omega_c}\frac{\partial f_0}{\partial r_g}\right), \tag{B10}$$

$$\mu^{TM}_{mnn'l}(s,\omega) = i16\pi^3 e^2 \tilde{k}^2_{mn'}\left(\frac{\omega}{c\tilde{k}_{mn}}\right)\left(\frac{\tilde{C}_{mn}}{\tilde{k}_{mn}}\right)\left(\frac{\tilde{C}_{mn'}}{\tilde{k}_{mn'}}\right)$$

$$\times \int r_g\, dr_g\, \frac{\tilde{k}_{mn}r_L}{l}\tilde{X}_{mnl-m}$$

$$\times \int p_\perp\, dp_\perp\, dp_z\, \frac{(\beta_z + ics/\omega)}{\omega - l\Omega_c/\gamma + isv_z}$$

$$\times\left(\tilde{X}_{mn'l-m}\frac{\partial f_0}{\partial p_\perp} + \frac{\tilde{Y}_{mn'l-m}}{m_0\Omega_c}\frac{\partial f_0}{\partial r_g}\right), \quad (B11)$$

$$\mu^{ME}_{mnn'l}(s,\omega) = i16\pi^3 e^2 k^2_{mn'}\left(\frac{\omega}{c\tilde{k}_{mn}}\right)\left(\frac{\tilde{C}_{mn}}{\tilde{k}_{mn}}\right)\left(\frac{C_{mn'}}{k_{mn'}}\right)$$

$$\times \int r_g\, dr_g\, \frac{\tilde{k}_{mn}r_L}{l}\tilde{X}_{mnl-m} \int p_\perp\, dp_\perp\, dp_z$$

$$\times\frac{(\beta_z + ics/\omega)}{\omega - l\Omega_c/\gamma + isv_z}\left[X_{mn'l-m}\right.$$

$$\times\left(\beta_z\frac{\partial f_0}{\partial p_\perp} - \beta_\perp\frac{\partial f_0}{\partial p_z}\right) - \beta_z\frac{Y_{mn'l-m}}{m_0\Omega_c}\frac{\partial f_0}{\partial r_g}\left.\right].$$
$$(B12)$$

By performing the integrals in Eqs. (B5)–(B12) for the distribution function defined in Eq. (23), the linearized amplitude equations correct to leading order in $c^2 k^2_{mn}/(\omega - l\Omega_c/\gamma - k_z v_z)^2$ can be expressed by Eqs. (44) and (45).

[1] Ya. L. Bogomolov, V. L. Bratman, N. S. Ginzburg, M. I. Petelin, and A. D. Yanokovsky, Opt. Commun. 36, 109 (1981).

[2] L. R. Ellis, G. Ramain, J. Hu, and A. Amir, Phys. Rev. Lett. 75, 424 (1986).

[3] T. M. Antonsen, Jr. and B. Levush, Phys. Rev. Lett. 62, 1488 (1989).

[4] K. E. Kreischer and R. J. Temkin, Phys. Rev. Lett. 59, 549 (1987).

[5] E. Jerby and A. Gover, Phys. Rev. Lett. 63, 864 (1989).

[6] R. A. Jong, W. M. Fawley, and E. T. Scharlemann, Proc. SPIE 1045, 18 (1989).

[7] R. A. Schill, Jr., Phys. Fluids B 2, 2798 (1990).

[8] R. A. Schill, Jr. and S. R. Seshadri, Phys. Fluids B 2, 2818 (1990).

[9] A. T. Lin, C.-C. Lin, and K. R. Chu, IEEE Trans. Electron Devices ED-36, 785 (1989).

[10] C. Chen and J. S. Wurtele, Phys. Rev. Lett. 65, 3389 (1990).

[11] V. L. Bratman, N. S. Ginzburg, G. S. Nusinovich, M. I. Petelin, and P. S. Strelkov, Int. J. Electron. 51, 541 (1981).

[12] A. W. Fliflet, Int. J. Electron. 61, 1049 (1986).

[13] R. W. Twiss, Aust. J. Phys. 11, 564 (1958).

[14] J. Schneider, Phys. Rev. Lett. 2, 504 (1959).

[15] A. V. Gapunov, Addendum. Izv. VUZ. Radiafiz. 2, 837 (1959).

[16] I. E. Botvinnik, V. L. Bratman, A. B. Volkov, N. S. Ginzburg, G. G. Denisov, B. D. Kol'chugin, M. M. Ofitserov, and M. I. Petelin, Pis'ma Zh. Eksp. Teor. Fiz. 35, 418 (1982) [JETP Lett. 35, 390 (1982)].

[17] J. G. Wang, R. M. Gilgenbach, J. J. Choi, C. A. Outten, and T. A. Spencer, IEEE Trans. Plasma Sci. PS-17, 906 (1989).

[18] G. Bekefi, A. DiRienzo, C. Leibovitch, and B. G. Danly, Appl. Phys. Lett. 54, 1302 (1989).

[19] A. DiRienzo, G. Bekefi, C. Chen, and J. S. Wurtele, Phys. Fluids B 3, 1755 (1990).

[20] K. R. Chu and J. L. Hirshfield, Phys. Fluids 21, 461 (1978).

[21] K. D. Pendergast, B. G. Danly, R. J. Temkin, and J. S. Wurtele, IEEE Trans. Plasma Sci. PS-16, 122 (1988).

[22] K. R. Chu and A. T. Lin, IEEE Trans. Plasma Sci. PS-16, 90 (1988).

[23] C. Chen and J. S. Wurtele, Phys. Rev. A 40, 489 (1989).

[24] J. A. Davies, Phys. Fluids B 2, 663 (1989).

[25] R. C. Davidson and H. S. Uhm, Phys. Fluids 29, 2713 (1986).

[26] R. G. Kleva, B. Levush, and P. Sprangle, Phys. Fluids B 2, 185 (1990).

[27] M. Abramowitz and I. A. Stegun, Handbook of Mathematical Functions (Dover, New York, 1972).

[28] P. Sprangle, C. M. Tang, and W. M. Manheimer, Phys. Rev. A 21, 302 (1980).

[29] K. R. Chu, A. T. Drobot, H. H. Szu, and P. Sprangle, IEEE Trans. Microwave Theory Tech. MTT-28, 313 (1980).

[30] V. L. Bratman, G. G. Denisov, N. S. Ginzburg, and M. I. Petelin, IEEE J. Quantum Electron. QE-19, 282 (1983).

[31] Y. Y. Lau, IEEE Trans. Electron Devices ED-29, 320 (1982).